Gravity affects magma-induced crustal deformation: comparing laccoliths on the Moon, Mars, and Earth

S. Poppe[1], A. Cornillon[1,2], A. Morand[1,3], and C. E. Harnett[4]

[1] Centrum Badań Kosmicznych Polskiej Akademi Nauk, Bartycka 18A, 00-716 Warsaw, Poland.
[2] Université Paris-Saclay, CNRS, GEOPS, Orsay, France.
[3] School of Earth Sciences, Bristol University, United Kingdom.
[4] UCD School of Earth Sciences, University College Dublin, Belfield, Dublin 4, Ireland.
*contact: sampoppe@cbk.waw.pl, sam35poppe@gmail.com

Please refer to this work in its final publication, in the meantime as:
Poppe, S., Cornillon, A., Morand, A., Harnett, C. (2024). Gravity affects magma-induced crustal deformation: comparing the Moon, Mars, and Earth. *Preprint, EarthArxiv*.

Gravity affects magma-induced crustal deformation: comparing the Moon, Mars, and Earth

S. Poppe[1], A. Cornillon[1,2], A. Morand[1,3], and C. E. Harnett[4]

[1]Centrum Badań Kosmicznych Polskiej Akademi Nauk, Bartycka 18A, 00-716 Warsaw, Poland. [2]Université Paris-Saclay, CNRS, GEOPS, Orsay, France. [3]School of Earth Sciences, Bristol University, United Kingdom. [4]UCD School of Earth Sciences, University College Dublin, Belfield, Dublin 4, Ireland.

Corresponding author: Sam Poppe (sampoppe@cbk.waw.pl and sam35poppe@gmail.com)

Key Points:

- We simulated magmatic laccolith inflation at the gravity of the Moon, Mars, and Earth with the two-dimensional Discrete Element Method.
- The simulated magma-induced fracturing accumulates in narrower zones in weaker rock at lower gravity.
- Laccolith inflation induces more vertical surface displacement at lower gravity and opens higher and wider cracks in the crust.

Abstract

Dome-shaped, uplifted surface areas and associated fractures on Mars and the Moon are inferred to result from the shallow emplacement of magma intrusions. This inference originates from analog observations of Earth's volcanic and igneous plumbing systems. Computational models help estimate those inferred magma bodies' geometry and emplacement depth. Such models have not yet simulated the dynamic fracturing of the host rocks at different gravitational accelerations on planetary bodies with different masses. We used the two-dimensional Discrete Element Method (2D DEM) to simulate the inflation of a laccolith, a magma body with a convex upward roof, in particle-based assemblages of different mechanical strengths, at the gravitational acceleration of the Moon, Mars, and Earth. The 2D DEM model simulates the host rock displacements, stresses, and dynamic fracturing, and allows calculating the finite shear strains and principal stresses. We find that in weak rocks the vertical surface displacement is nearly twice as high on the Moon, compared to Earth. Only half as many cracks are generated in strong rocks on the Moon compared to on Earth. Our 2D DEM simulations show, for the first time, that gravity specific to a rocky planetary body affects both the pattern and the amount of fracturing and surface displacement above inflating laccoliths. These findings call for a careful reevaluation of differences seen in the morphology of intrusive domes found on Earth, Mars, and the Moon.

Plain Language Summary

Domed and fractured surface areas have been observed on the Moon and Mars. Similar features in volcanic areas on Earth suggest they may have been caused by laccoliths – magma intrusions with a convex roof and horizontal base – at shallow crustal levels. Gravitational acceleration depends on a planetary body's mass, being lower on the Moon than on Mars, and lower on Mars than on Earth. Do laccoliths of similar dimensions and emplacement depth cause comparable patterns of displacement and fracturing across these bodies? Using the two-dimensional Discrete Element Method, we simulated the displacement and progressive fracturing of host rocks around inflating laccolith intrusions under lunar, Martian, and Earth gravities. We found that weaker gravity leads to more surface displacement from similar-volume laccoliths. The amount of magma-induced fracturing, however, depends more on host rock strength than on gravity. Thus, both gravity and crustal strength affect laccolith-induced deformation patterns and need to be considered when inferring magma intrusion properties from surface observations on rocky planets and moons.

1 Introduction

Dome-shaped surface features in volcanic terrains on Earth have been related to the emplacement of thick magma intrusions in the shallowest several kilometers of the crust (Bunger & Cruden, 2011; Gilbert, 1877; Morgan, 2018; Pollard & Johnson, 1973). Such thick intrusions include laccoliths (intrusions with a horizontal base and a convex-upward roof) and sills (tabular, often horizontal, intrusions between preexisting layers of rock). Geological and geophysical observations have shown that the crustal stresses associated with the inflation of these intrusions induce displacement, bending, compaction, fracturing and faulting of the host rocks, and a dome-shaped uplift pattern at the surface (e.g., Mattsson et al., 2018; Wilson et al., 2016).

Surface displacements and fracturing are the only visible indicators of laccolith emplacement on other planetary bodies. The magmatism on both Mars and the Moon is considered dominantly mafic with a low viscosity (Head & Wilson, 2017; Platz et al., 2015; Vaucher et al., 2009). There, many areas with a dome-shaped positive topography have rough surfaces and lie adjacent to apparent eruptive cones, pyroclastic deposits and thick lava flows that suggest they are the result of the extrusion of felsic, viscous lava (Brož et al., 2015; Farrand et al., 2021; Ivanov et al., 2016; Lena et al., 2013; Wilhelms, 1987). Some, however, have a gentle slope, open fractures and no eruptive vents and are likely induced by magma emplacement in the shallowest few kilometers of the lunar crust without eruption (Head & Wilson, 2017; Lena et al., 2013; Wöhler & Lena, 2009). Known examples of lunar intrusive domes are the Valentine domes in Mare Serenitatis (Fig. 1a). Lunar intrusive domes range in diameter from less than one kilometer to more than 30 kilometers (Lena et al., 2013). On Mars, no global-scale overview exists to date, but intrusive domes have been found in association with cryptodomes or laccoliths exposed by erosion (Fig. 1b) in regions with distributed volcanism away from the largest Martian volcanoes (Farrand et al., 2011; Platz et al., 2015; Rampey et al., 2007).

The relative scarcity of intrusive domes is explained by the negative buoyancy of dense mafic magma in the shallowest kilometres of the less dense lunar crust, which is dominantly composed of anorthosite and highly porous rocks due to a long impact history (Wieczorek et al., 2013; Wöhler & Lena, 2009). Lunar intrusive domes also often lie in areas between proximal mare-filled impact basins, where crustal extensional stresses might favor the ascent of buoyant magma into shallower crustal levels (McGovern et al., 2014; Thomas et al., 2015). Models have confirmed the likely formation of cryptodomes and laccoliths at Arcadia Planitiae, albeit in interaction with now-molten ice sheets (Farrand et al., 2011; Michaut et al., 2013).

Other sites of inferred magma-induced surface doming and fracturing on Mars and the Moon are ´floor-fractured craters´ (FFCs) (Fig. 1d, 1e) (Jozwiak et al., 2012; Michaut, 2011; Schultz, 1976). Floor-fractured crater morphology has been explained by post-impact viscous relaxation of the crust (Bamberg et al., 2014; Hall & Solomon, 1981; Montigny et al., 2022). Observations of gravity anomalies by NASA´s Gravity Recovery and Interior

Laboratory (GRAIL) have instead confirmed the shallow presence of dense magma intrusions below lunar floor-fractured craters (Wieczorek et al., 2013). Models have shown that impact cratering provides a lithospheric stress deficit and driving overpressure for magma to ascend below the crater floor (Michaut & Pinel, 2018). There, the magma may then have inflated a sill or laccolith and further fractured and uplifted the overburden rocks (Michaut et al., 2020; Michaut & Pinel, 2018; Wöhler & Lena, 2009).

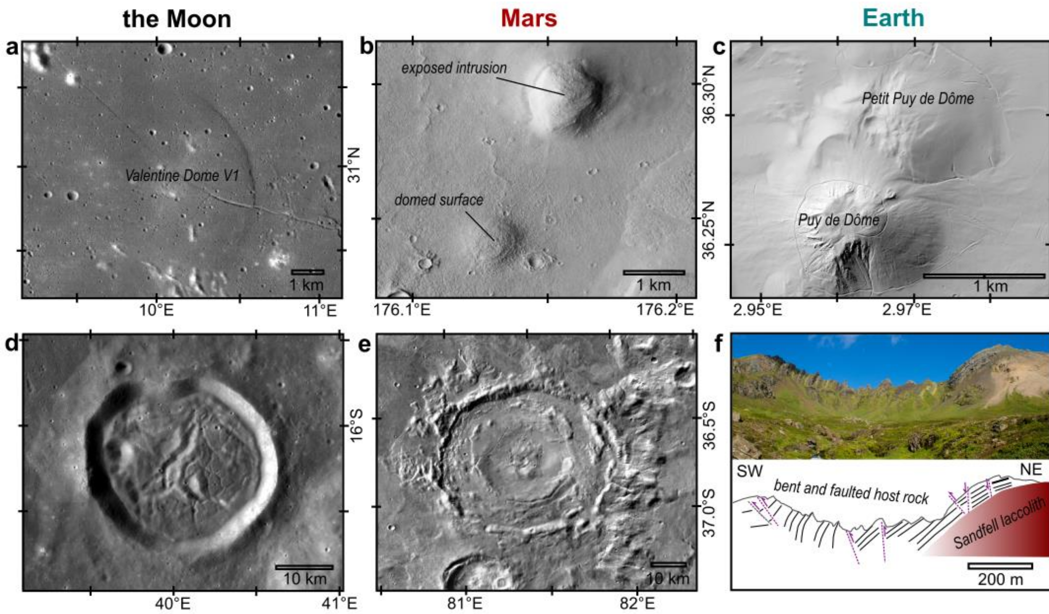

***Fig. 1** Magma-induced dome-shaped uplift features on three planetary bodies of different mass: **a.** Valentine 1 dome in Mare Serenitatis on the Moon (Lunar Reconaissance Orbiter (LRO), NASA); **b.** domed surface feature and exposed intrusion East of Phlegra Montes on Mars (Context Camera (CTX), NASA); **c.** hillshade relief image of the intrusive dome Petit Puy de Dôme and extrusive lava dome Puy de Dôme, Chaine-des-Pûys, France (LIDAR dataset www.craig.fr); **d.** lunar floor-fractured crater Bohnenberger (LRO, NASA); **e**. martian floor-fractured crater 28-000072 (Themis, NASA); **f.** image and interpretive sketch of the exposed Sandfell laccolith and bent and faulted host rocks in East-Iceland (after Mattsson et al., 2018).*

The scarcity of recent and well-monitored laccolith intrusion events on Earth makes understanding their intrusion dynamics challenging. The 2011-2012 rhyolitic laccolith emplacement and explosive eruption at Puyehue Cordón Caulle, in Chile, is the only recent monitored event where seismicity and dome-shaped surface uplift and tensile surface fracturing was recorded (Castro et al., 2016). Understanding laccolith emplacement dynamics thus relies on studying now-solidified and exposed volcanic and igneous plumbing systems on Earth, or on modeling (Bunger & Cruden, 2011; Galland et al., 2018; Magee et al., 2018; Morgan, 2018). Dome-shaped, uplifted surfaces are often heavily discretised by faults and fractures, such as at the Petit Puy de Dôme in the Chaîne des Puys volcanic field in France (Fig. 1c) (Petronis et al., 2019). Geological observations at terrestrial laccoliths, such as at Sandfell in Iceland (Fig. 1f), show the importance of discontinuous fracturing and faulting of the overlying rocks, besides elastic bending (Mattsson et al., 2018; Wilson et al., 2016).

The dynamics of how the crustal displacement and fracturing relates surface displacements and fracturing to an inflating laccolith at depth remains unclear. This is partly because existing analytical and numerical models assume a linearly-elastic response of the lunar and martian crust to magma-induced stresses in a continuous and homogeneous half-space (Bunger & Cruden, 2011; Grosfils et al., 2015; Michaut, 2011; Michaut & Pinel, 2018; Pollard & Johnson, 1973; Thorey & Michaut, 2016; Wöhler & Lena, 2009). Linearly-elastic behavior implies that rocks deform instantaneously and proportionally to stress, and may reverse to its initial state once the stress source is removed. Once the critical stress is exceeded, tensile fractures open and the rock ruptures (Jaeger et al., 2007; Segall, 2010). Some models have implemented more complex stress responses, such as elasto-plastic behaviour in Finite Element Models (FEM), but still do not represent the dynamic cracking process (Carrier et al., 2015; Daniels et al., 2012; Gerbault et al., 2018; Haug et al., 2017; Scheibert et al., 2017).

The role of non-elastic deformation in shaping laccolith- and sill-induced fractures and faults has been documented in scaled laboratory experiments, where surface deformation can be directly related to the intrusion of analog magma in granular, cohesive materials (Currier & Marsh, 2015; Montanari et al., 2017; Poppe et al., 2019; Schmiedel et al., 2017). Furthermore, magnetic crystal fabrics in now-solidified and exposed viscous magma in Iceland and Argentina show that laccoliths can grow through repetitive magma pulses of high ascent rates and week- to month-long pauses during which the magma partially cools and solidifies (Burchardt et al., 2019; Mattsson et al., 2018). Crustal displacement, straining and fracturing then often allows for major widening and thickening of sills and laccoliths without eruption.

Accounting for nonelastic deformation and dynamic fracturing during laccolith inflation may be especially impactful for other rocky planets and moons in our Solar System. There, lower global mass results in lower gravitational acceleration compared to that on Earth. Compilations of rock deformation experiments have shown that reduced surface gravity leads to increased porosity and, consequentially, reduced brittle and tensile strength for similar depths (Heap et al., 2017). Models that assume linear elasticity during laccolith inflation (Bunger & Cruden, 2011; Michaut & Pinel, 2018; Walwer et al., 2021; Wöhler & Lena, 2009), can thus not clarify what the effect is of specific gravity on the development of crustal fracturing and surface displacements during the inflation of a laccolith.

High concentrations of strain, and dynamic fracturing, can be simulated in the Discrete Element Method (DEM) (Cundall & Strack, 1979; Potyondy & Cundall, 2004). The DEM discretizes a medium into an assemblage of rigid disks or spheres of which the position at each timestep is calculated according to Newton's laws of motion (Cundall & Strack, 1979). Unlike FEMs, the DEM allows for the concentrations of large strains, discontinuous deformation and the dynamic opening and propagation of tensile fractures and shear bands. The particle assembly can thus be calibrated to respond mechanically similar to natural rock (Cundall & Strack, 1979; Potyondy & Cundall, 2004; Schöpfer et al., 2009). DEM has been used to simulate, amongst others, lava dome effusion and stability, hydraulic fracture propagation, or caldera collapse (Harnett et al., 2020; Harnett & Heap, 2021; Holohan et al., 2015; Huang et al., 2022; Morgan & McGovern, 2005; Woodell et al., 2023).

Simulating viscous fluid intrusion in the DEM requires complex and computationally expensive coupling with other methods (Schöpfer & Lehner, 2024; Wang et al., 2022). Instead, highly viscous fluid intrusion can be simulated in 2D DEM models by injecting particles upwards from a conduit into the host rock assemblage (Meng & Hodgetts, 2020; Morand et al., 2024). Meng & Hodgetts (2020) found that viscous sand-water injectites may induce differential host rock compaction, localized deformation without major surface displacements in soft sediments (Young´s modulus E = 2.2 GPa, unconfined compressive strength UCS = 0.4 MPa), and forced folding and tensile surface fracturing in stiffer sediments (E = 21.8 GPa, UCS = 2.0 MPa). However, they only evaluated major fracture patterns and contact force chains. Morand et al. (2024) evaluated displacements, principle stresses, finite strains and crack patterns in a wider range of host rock strengths (E = 2.5 – 30.0 GPa, UCS = 7.0 – 203.0 MPa) induced by laccolith inflation at different depths (0.5 – 1.5 km). They showed that the deformation pattern varies between two end-members depending on the host rock strength: (a) extensive fracturing, wide zones of shear strain, multiple tensile surface fractures in stiff rocks mostly above a shallower source; or (b) scarce fracturing, narrow zones of shear strain and a single central surface fracture in tough rocks above a deeper source. It is unknown if these findings remain valid on other planetary bodies with a different gravitational acceleration than Earth´s.

We present 2D DEM simulations of the inflation of a laccolith at 1.5 kilometer depth under gravitational acceleration for Earth, Mars and the Moon in a 2D DEM model. We vary the strength of the host particle assemblage to represent a range of plausible planetary crustal strengths. Our work expands on the existing DEM results by simulating the effect of gravity specific to planetary bodies of different mass and crustal strength on the magma-induced dynamic fracturing, along with displacement and strain patterns. Our findings reveal how the relationship between a shallow inflating laccolith and the extent and magnitude of surface displacements and fracturing depends on crustal strength and a planetary body´s specific gravity.

2 Method

2.1 Model set-up and boundary conditions

We implemented the inflation of a laccolith in the two-dimensional (2D) DEM Particle Flow Code (PFC2D 7.0) from Itasca Consulting Group, Ltd. (https://www.itascacg.com/software/PFC). We followed the method of settling a stable particle assemblage as described by Harnett & Heap (2021) and Morand et al. (2024).

Spherical particles with radii normally distributed around a mean of 8.66 ± 1.66 m were generated in a rectangular model domain of 20 km wide and 1 km high, constrained by lateral and bottom platens ('walls') and with a free upper surface (Fig. 2). The particles are rigid disks with a density of 2500 kg.m^{-3} that cannot deform internally. Particles interacted with neighbouring particles and the model walls. We assigned particles to a rock class or a magma class.

Contact bonds of a rock particle with neighbouring rock particles or a wall were governed by the soft-bond model (Jiang et al., 2015; Ma & Huang, 2018a). The strength and behavior of soft bonds is defined by a bond effective modulus E*, a bond tensile strength, a bond cohesion, and two softening parameters (Ma & Huang, 2018b). All other particle bond parameters were kept constant (see Table S1 in the Supporting Information). The two softening parameters were kept constant to approach a 10:1 ratio of unconfined compressive strength to tensile strength in the numerical rock. This ensures that contacts break when their tensile strength is exceededClick or tap here to enter text.. The contact behavior at a broken bond is then governed by friction.

Magma particles were assigned within a 1,000 m-wide body with a horizontal base and a half-ellipse-shaped convex roof with a maximum thickness of 50 m (Fig. 2). This laccolith was centered at the bottom of the model with its top at 1,000 m below the upper free surface. Contacts between two magma particles, between a rock and magma particle, and between magma particles and the bottom wall were defined by the linear parallel bond model, with zero friction, zero cohesion, zero tensile strength but a high effective modulus E*. This approach approximates the behavior of incompressible magma (Morand et al., 2024).

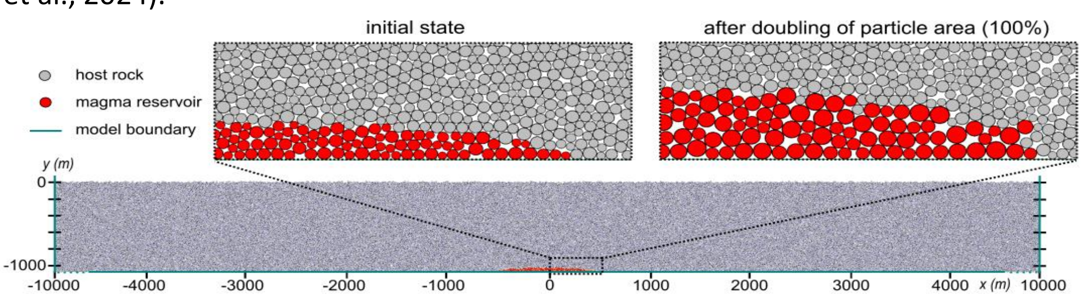

Fig. 2 *Model set-up implemented in the two-dimensional Discrete Element Method (2D DEM) in PFC2D (Itasca Ltd.) with an assemblage of host rock particles (grey) and a particle-based, half-ellipsoid-shaped magma body (red) with its top at 1.5 km depth. The subset images display the initial state and final state of the magma body after doubling of the magma particle area, i.e. after 100% of laccolith inflation.*

2.2 Mechanical properties

We simulated a range of plausible strengths of planetary crust, not one particular strength of host rock. This approach supports our aim to study laccolith-induced deformation as a function of gravitational acceleration and crustal strength. In the DEM, the absolute values of the rock particle soft-bond parameters differ from the strength values of the bulk rock. The particle bond values affect two properties of the rock strength. The toughness relates to the resistance of the rock to cracking and is mainly controlled by the bond cohesion and bond tensile strength. Tougher rocks can accommodate more strain before breaking. The stiffness relates to the resistance of the rock to elastic bending, and is mainly controlled by the bond effective modulus and ratio of normal to shear stiffness. Overall, stiffer rocks require more force to obtain a given amount of displacement and strain.

To obtain the particle bond effective modulus, bond cohesion and bond tensile strength that define the desired bulk properties, we computed uniaxial 2D DEM tests in PFC2D (Harnett & Heap, 2021; Ma & Huang, 2018a; Morand et al., 2024). Uniaxial compressive tests helped define the average unconfined compressive strength (UCS) and Young´s modulus (E). Uniaxial extension tests helped define the tensile strength (TS). Methodological details and the individual test results are provided in the Supporting Information.

Rock mass strength parameters on Earth are typically derived from laboratory tests on intact rock samples. By compiling data from deformation experiments on terrestrial basalts, Heap et al. (2017) showed that even at depths shallower than -5 km the brittle strength of the Martian crust is lower than on Earth but can vary considerably from 20 – 400 MPa depending on the physical attributes of the basalt. The obtained properties overestimate the bulk strength of the crust because the tested samples do not capture fracture networks, pore water saturation and other large-scale discontinuities (Harnett et al., 2023). Geotechnical properties of intact samples can be upscaled to the rock mass using field-based rock mass characterization; such efforts have shown the brittle strength of the crust can be up to ten times weaker than that of intact rock samples (Heap et al., 2020; Villeneuve & Heap, 2021). Rock mass characterization remains challenging for lunar and Martian crust, even if Klimczak (2015) estimated a similar Geological Strength Index for the Martian lithosphere compared to Earth´s. Existing analytical models have assumed a Young´s modulus of 1-10 GPa (Michaut et al., 2013; Thorey & Michaut, 2014), with others as high as 70-100 GPa (Michaut, 2011; Wohler et al., 2009). Crustal bulk stiffness has been shown to more likely approach a lower Young´s modulus below 10 GPa (Heap et al., 2020).

We therefore explored the effect of gravity on laccolith-induced deformation across a range of realistic crustal strengths, governed by an effective bond modulus of 3 or 10 GPa, and bond tensile strength of 1, 2.5 or 5 MPa (Table 1). The bond cohesion was kept at ten times that of the bond tensile strength to maintain UCS:TS ratios between 8 and 12 that are typical in laboratory tests on intact rocks (Jaeger et al., 2007; Heap et al., 2021). We simulated six combinations of three rock toughnesses (TS of 0.8 ± 0.1 MPa, 1.9 ± 0.2 MPa, or 3.7 ± 0.1 MPa) for two rock stiffnesses (Young´s modulus of 2.5 ± 0.1 GPa or 8.4 ± 0.1 GPa). Figures 3-6 only display the bulk strength values (E, UCS, TS) for comparison with natural rock strengths, Table 1 displays the relations with the bond strengths in the numerical model.

2.3 Model exploitation and analysis

We aimed to investigate the effect of the inflation of a laccolith on the shallow crust in function of gravity. We thus ran 2D DEM simulations that are subjected to the gravitational acceleration constant g of Earth (9.81 $m.s^{-2}$), Mars (3.71 $m.s^{-2}$), or the Moon (1.62 $m.s^{-2}$). We incrementally increased the area of the circular magma particles in the laccolith in steps of 1% until an area inflation of 100% was obtained (Fig. 2). Assuming an axial intrusion symmetry, this represents the doubling of laccolith volume from ~0.1 km^3 to ~0.2 km^3. This approach of particle area change is similar to that used to simulate the deflation of a magma body (Holohan et al., 2011, 2015), but differs from that of Harnett et al. (2020) and Morand et al. (2024), wherein new particles were added from below to inflate the lava dome or laccolith.

The inflating laccolith exerted stress on the surrounding rock particles, which were displaced. As a consequence, rock-rock contacts were strained. Particles resisted relative rotation which simulated a rigid interface between them. Once strained rock particle bonds failed, the soft-bond model was replaced by a rolling-resistance model that was only governed by a friction coefficient of 0.5 but with no bond cohesion or bond tensile strength. A crack was thus formed where a bond broke. This enabled the DEM to simulate the strain-induced opening of tensile cracks, complex fracturing patterns, large discontinuous strains and displacement of the detached rock masses along fracture planes typically seen in exposed laccolith roofs.

Particle position, velocity, displacement, bond stresses and bond cracking were tracked throughout the model. By convention, upward and rightward displacements are positive; downward and leftward displacements are negative. We express the number of cracked bonds as a percentage of the initial amount of rock particle bonds. In post-processing, the displacement gradient tensor is used to determine the finite shear strain from the Cauchy-Green deformation tensor (Schöpfer et al., 2006), further described by Harnett et al. (2018) and Morand et al. (2024). Less than 10% of particles have particularly high strains, for example where a particle detached from the surface and rolled down in an open crack. Because these large strains hide the smaller strains that provide insight in the laccolith-induced deformation patterns, we apply a cut-off criterion in our model visualization. All finite shear strain values higher than 0.05% are set to 0.05%. We then normalize all finite shear strain values to the simulation´s maximum to emphasize the relative shear strain distribution within a simulation. The maximum lateral extent of the vertically displaced surface includes all surface particles that are vertically displaced by more than 0.5% of the maximum vertical displacement value detected in the final time step of the simulation.

3 Results

3.1 Influence of gravity on magma-induced deformation

We systematically analyzed the patterns of magma-induced displacement (Fig. 3), and of vertical and horizontal displacement at the surface (Fig. 4). The Supporting Information provides the final model outcomes, the total displacements, stress, strain, and crack patterns.

Regardless of the specific gravity, the displaced rock areas are laterally delimited by one or more en-echelon fracture zones. Those fracture zones dip the steepest in the least tough rocks (TS 0.8 ± 0.1 MPa) (Fig. 3a-c, 3j-l) and the most gentle in tough rocks (TS 3.7 ± 0.4 MPa) (Fig. 3g-i, 3p-r). Consequently, in the toughest rocks the displaced area of rock is the widest (Fig. 3g-i, 3p-r), the displacement magnitude decreases continuously laterally away from the centre (x = 0), the longest and widest fractures are generated, and also the displaced zones at the surface are the widest (Fig. 4i-l). The least tough rocks display discontinuities along which the displacement magnitude abruptly decreases away from the model centre (x = 0) (Fig. 3a-i), and the vertical and horizontal surface displacements vary stepwise (Fig. 4a-h). The locations of those stepwise variations correspond to open fractures at the model surfaces.

Table 1. *Summary of bond strength and bulk strength values and key results for the 18 performed 2D DEM simulations.*

Model setup	***Bond parameters***			***Mechanical properties***				***Model results***		
Gravity g ($m.s^{-2}$)	**E* (GPa)**	**Coh (MPa)**	**Ten (MPa)**	**E (GPa)**	**UCS (MPa)**	**TS (MPa)**	**UCS/ TS**	**Final U_y^{max} (m)**	**Lateral extent of U_y (km)**	**Fracture pattern End-member**
-1.62	3.0	10.0	1.0	2.5 ± 0.1	6.6 ± 0.9	0.8 ± 0.1	8.3 ± 2.0	40.0	3.699	Type 1
-3.71	3.0	10.0	1.0	2.5 ± 0.1	6.6 ± 0.9	0.8 ± 0.1	8.3 ± 2.0	36.9	3.903	Type 1
-9.81	3.0	10.0	1.0	2.5 ± 0.1	6.6 ± 0.9	0.8 ± 0.1	8.3 ± 2.0	26.1	4.330	Type 1
-1.62	3.0	25.0	2.5	2.5 ± 0.1	19.8 ± 3.5	1.9 ± 0.2	10.4 ± 2.6	46.3	4.735	Type 1
-3.71	3.0	25.0	2.5	2.5 ± 0.1	19.8 ± 3.5	1.9 ± 0.2	10.4 ± 2.6	37.2	4.328	Type 1
-9.81	3.0	25.0	2.5	2.5 ± 0.1	19.8 ± 3.5	1.9 ± 0.2	10.4 ± 2.6	28.0	4.211	Type 1
-1.62	3.0	50.0	5.0	2.5 ± 0.1	43.6 ± 6.0	3.7 ± 0.4	11.8 ± 2.6	40.4	5.723	Type 2
-3.71	3.0	50.0	5.0	2.5 ± 0.1	43.6 ± 6.0	3.7 ± 0.4	11.8 ± 2.6	37.6	4.670	Mixed
-9.81	3.0	50.0	5.0	2.5 ± 0.1	43.6 ± 6.0	3.7 ± 0.4	11.8 ± 2.6	37.2	4.191	Mixed
-1.62	10.0	10.0	1.0	8.4 ± 0.2	6.6 ± 0.9	0.8 ± 0.1	8.3 ± 2.0	43.5	3.537	Type 1
-3.71	10.0	10.0	1.0	8.4 ± 0.2	6.6 ± 0.9	0.8 ± 0.1	8.3 ± 2.0	40.0	3.942	Type 1
-9.81	10.0	10.0	1.0	8.4 ± 0.2	6.6 ± 0.9	0.8 ± 0.1	8.3 ± 2.0	35.6	3.821	Type 1
-1.62	10.0	25.0	2.5	8.4 ± 0.2	19.8 ± 3.5	1.9 ± 0.2	10.4 ± 2.6	42.5	4.923	Type 1
-3.71	10.0	25.0	2.5	8.4 ± 0.2	19.8 ± 3.5	1.9 ± 0.2	10.4 ± 2.6	38.0	4.242	Type 1
-9.81	10.0	25.0	2.5	8.4 ± 0.2	19.8 ± 3.5	1.9 ± 0.2	10.4 ± 2.6	39.5	3.791	Type 1
-1.62	10.0	50.0	5.0	8.4 ± 0.2	43.6 ± 6.0	3.7 ± 0.4	11.8 ± 2.6	39.5	7.813	Type 2
-3.71	10.0	50.0	5.0	8.4 ± 0.2	43.6 ± 6.0	3.7 ± 0.4	11.8 ± 2.6	42.3	4.702	Type 1
-9.81	10.0	50.0	5.0	8.4 ± 0.2	43.6 ± 6.0	3.7 ± 0.4	11.8 ± 2.6	39.1	4.045	Type 1

Regardless of the rock strength, the fracture zones that laterally delimit the displaced rock dip the steepest for the highest gravity (Earth) (e.g., Fig. 3i) and dip the most gentle for the lowest gravity (the Moon) (e.g., Fig. 3g). At the lowest gravity, those delimiting fractures propagate horizontally away from the inflating laccolith, the displaced area is the widest (Fig. 3g, 3p), the maximum of the displacement magnitude is the highest (~40 m), the extent of displacement at the surface is the widest and the slope of the vertical surface displacement curve is declining the steepest away from the center (x = 0) (Fig. 4, black curves). Under that lowest gravity, the stepwise variations in horizontal displacement are also the largest across open surface fractures (Fig. 4b, 4d, 4f, 4h). In the least tough rocks (TS 0.8 ± 0.1 MPa), the maximum of vertical displacement is 10-15 m higher at the Moon´s lower gravity than at Earth´s higher gravity (Fig. 4a, 4e); the maximum of horizontal displacement is 4-6 m lower on the Moon than on Earth (Fig. 4b, 4f). There is less difference in absolute displacement values at the domes´ crests for stronger rocks across gravities (Fig. 4g-l). Displacement magnitudes and surface displacements for the intermediate gravity specific to Mars are overall intermediary between those on the Moon and on Earth. Only for Earth´s higher gravity we observe a central graben, a depressed block near the surface delimited by normal faults with less positive vertical displacement than the dome flanks and near-zero horizontal displacement (Fig. 4a-f).

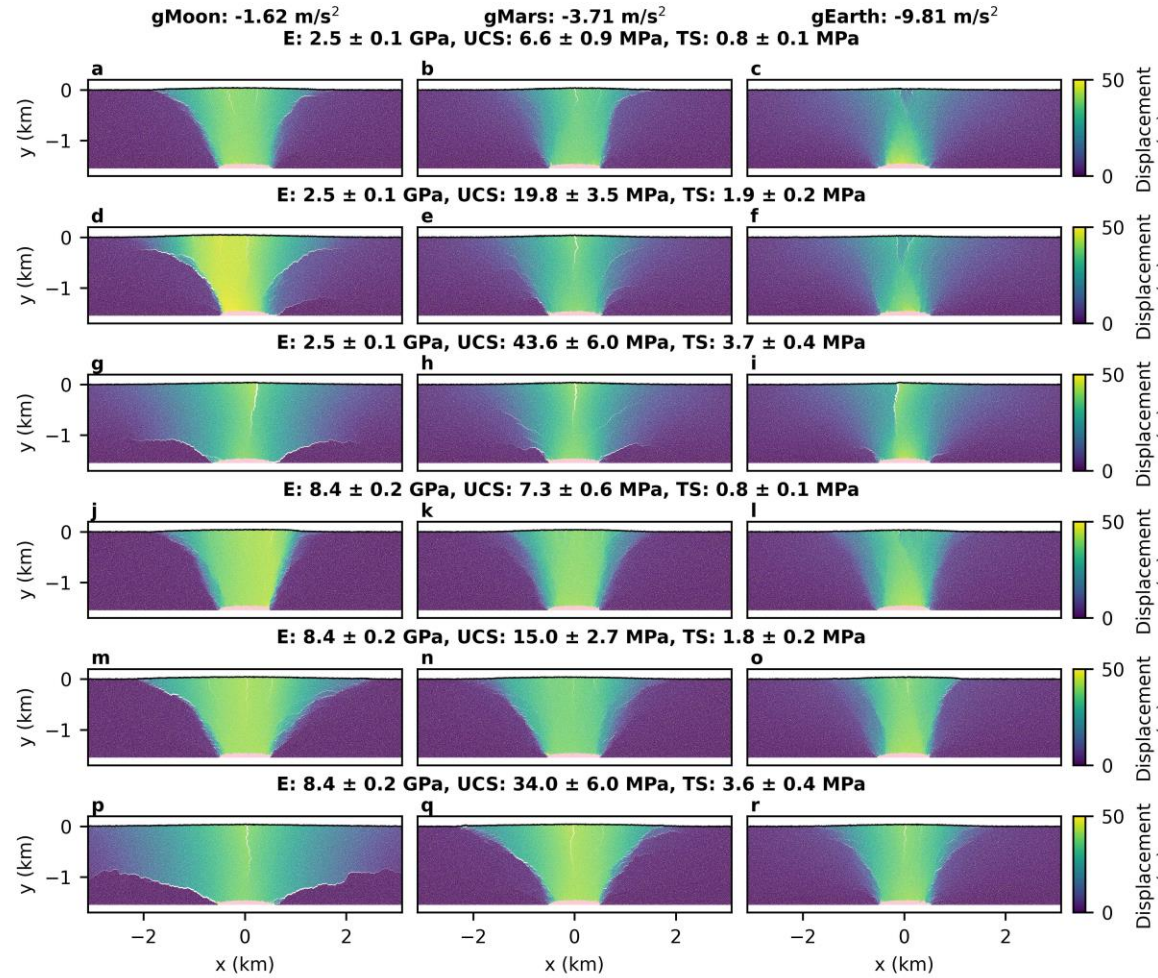

Fig. 3 *Displacement magnitude after doubling of the magma body area in the 2D DEM simulations subjected to gravity specific to the Moon, Mars, or Earth for a range of host rock Young´s moduli (E), unconfined compressive strengths (UCS) and tensile strengths (TS). Specific gravity increases from left to right, rock strength increases from top to bottom. Rock stiffness is the lowest in the three top rows and the highest in the three bottom rows.*

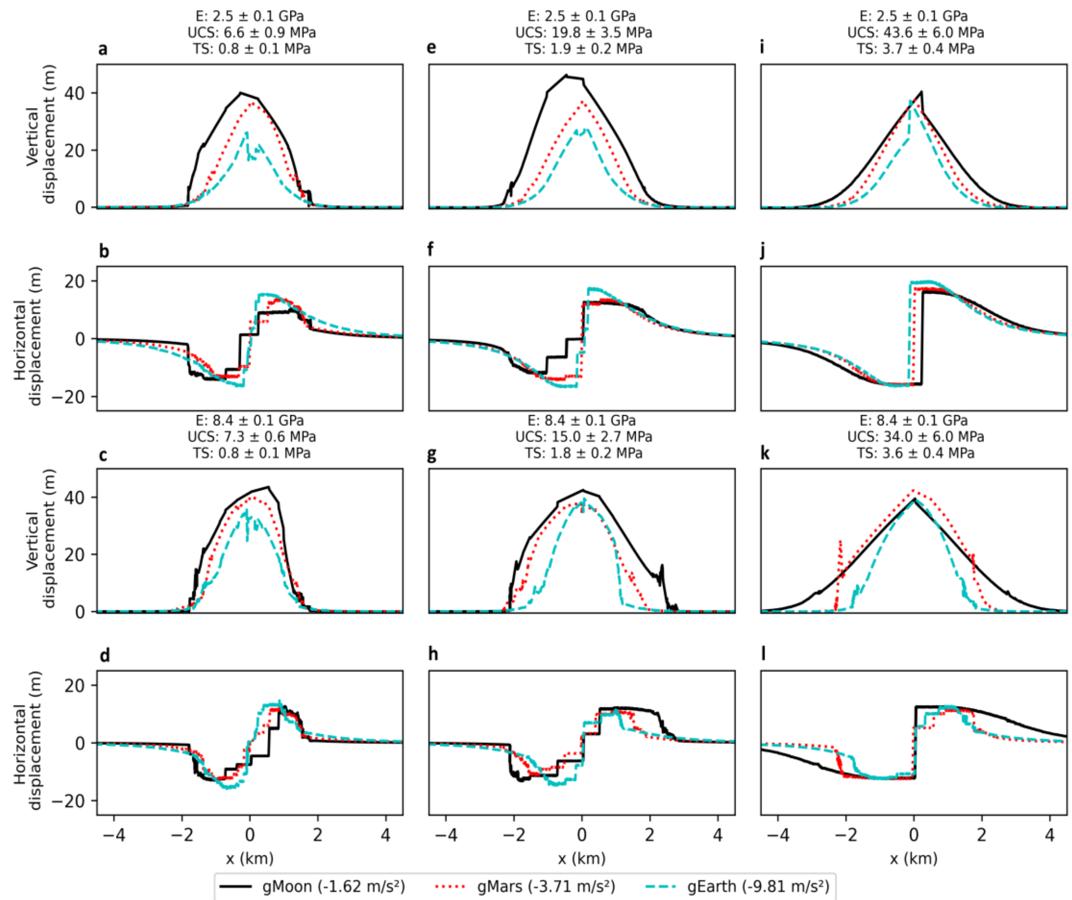

Fig. 4 *Horizontal and vertical surface displacement after doubling of the magma body area in 2D DEM simulations subjected to gravity specific to the Moon (black), Mars (red), or Earth (blue) for a range of host rock Young´s moduli (E), unconfined compressive strengths (UCS) and tensile strengths (TS). Toughness increases from the left column to the right column, stiffness increases from the top two rows to the bottom two rows. Gravity specific to each planetary body is indicated by line color and dashing.*

3.2 Influence of gravity on magma-induced strain and cracking

Regardless of specific gravity but for the same stiffness, less tough rocks (TS 0.8 ± 0.1 MPa) accumulate shear strain in narrower zones and generate the most cracks (Fig. 5a-c, 5j-l). Tough rocks (TS 3.7 ± 0.4 MPa) accumulate higher shear strain values (red-purple color) in wider zones and generate less cracks (Fig. 5g-i, 5p-r). As observed above, the fracture zones that delimit the deformed rock zone above the inflating laccolith are steeper in less tough rocks (Fig. 5a-c, 5j-l), and low-angle to subhorizontal in tough rocks (Fig. 5g-i, 5p-r). Quantitatively, up to 3.5% of bonds crack in less stiff rocks (E 2.5 ± 0.1 GPa) (Fig. 6a-c); up to 6.5% of bonds crack in stiff rocks (E 4.8 ± 0.1 GPa) (Fig. 6d-f). For the same stiffness, more cracks open in less tough rocks (4.5% – 6.5%) (Fig. 6a, 6d), less cracks open in tough rocks (0.5% – 2.5%) (Fig. 6c, 6f).

We observe a dependency of the amount of normalized finite shear strain and cracking on specific gravity. For the same stiffness, rocks accumulate shear strain in narrower zones with more gentle to subhorizontal dips and generate the least cracks at the Moon´s lower gravity (Fig. 5a, 5d, 5g, 5j, 5m, 5p). Rocks accumulate higher shear strain in wider zones with steeper dips and generate the most cracks at Earth´s higher gravity (Fig. 5c, 5f, 5i, 5l, 5o, 5r). Time series of finite shear strain and crack pattern development (see Supplementary videos) show that the tensile surface fractures at the crest of the uplifted surface propagate the deepest with the widest opening at the lowest gravity (compare e.g., Fig. 5g-I, or Fig. 5p-r). At Earth´s higher gravity and in stiff rocks (E 8.4 ± 0.2 GPa), bands of high finite shear strain ahead of tensile surface fractures remain uncracked (x = 0 to 1 km, y = 0 to -1 km, Fig. 5r).

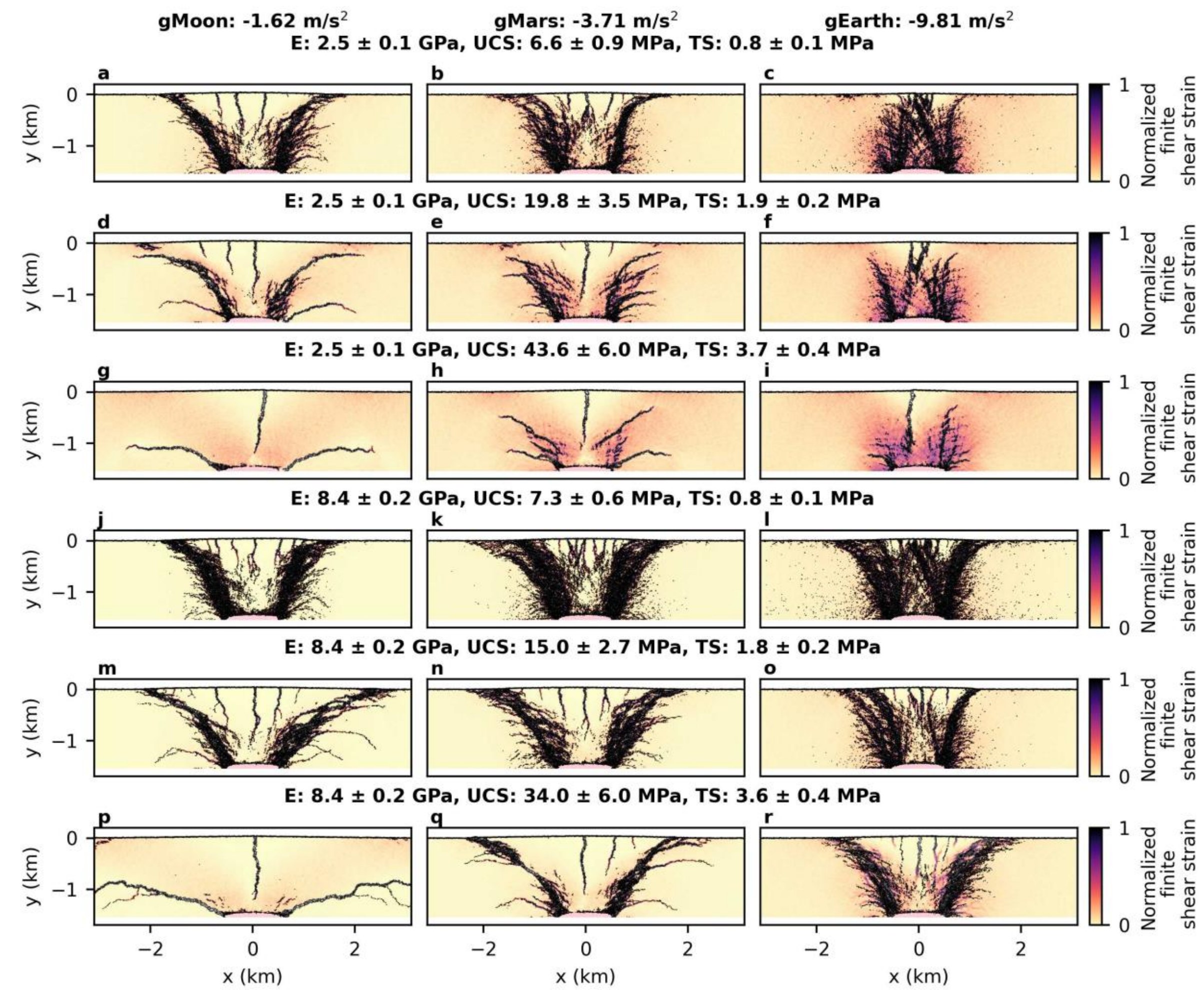

Fig. 5 *Normalized finite shear strain (see color bars) and cracked particle bonds (black lines) after doubling of the magma body area in the 2D DEM simulations subjected to gravity specific to the Moon, Mars, or Earth for a range of host rock Young´s moduli (E), unconfined compressive strengths (UCS) and tensile strengths (TS).*

Quantitatively, less cracks open at the Moon´s lower gravity (Fig. 6, black curves), compared to Earth´s higher gravity (Fig. 6, blue curves). Weak rock generates more cracks more rapidly when stressed at lower gravity (Fig. 6a). Strong rock generates more cracks more rapidly at higher gravity (Fig. 6b-c, 6e-f). The difference between the amount of cracks in function of gravity is the highest at 2% for the strongest rocks (Fig. 6f). Notably, there is no significant difference in the amount of cracks in function of specific gravity in weaker rocks (Fig. 6a), but the spatial fracture and shear strain pattern is markedly different (Fig. 5a-c). Overall, Martian rocks respond in an intermediate manner to the inflation of the laccolith, compared to those on the Moon and Earth.

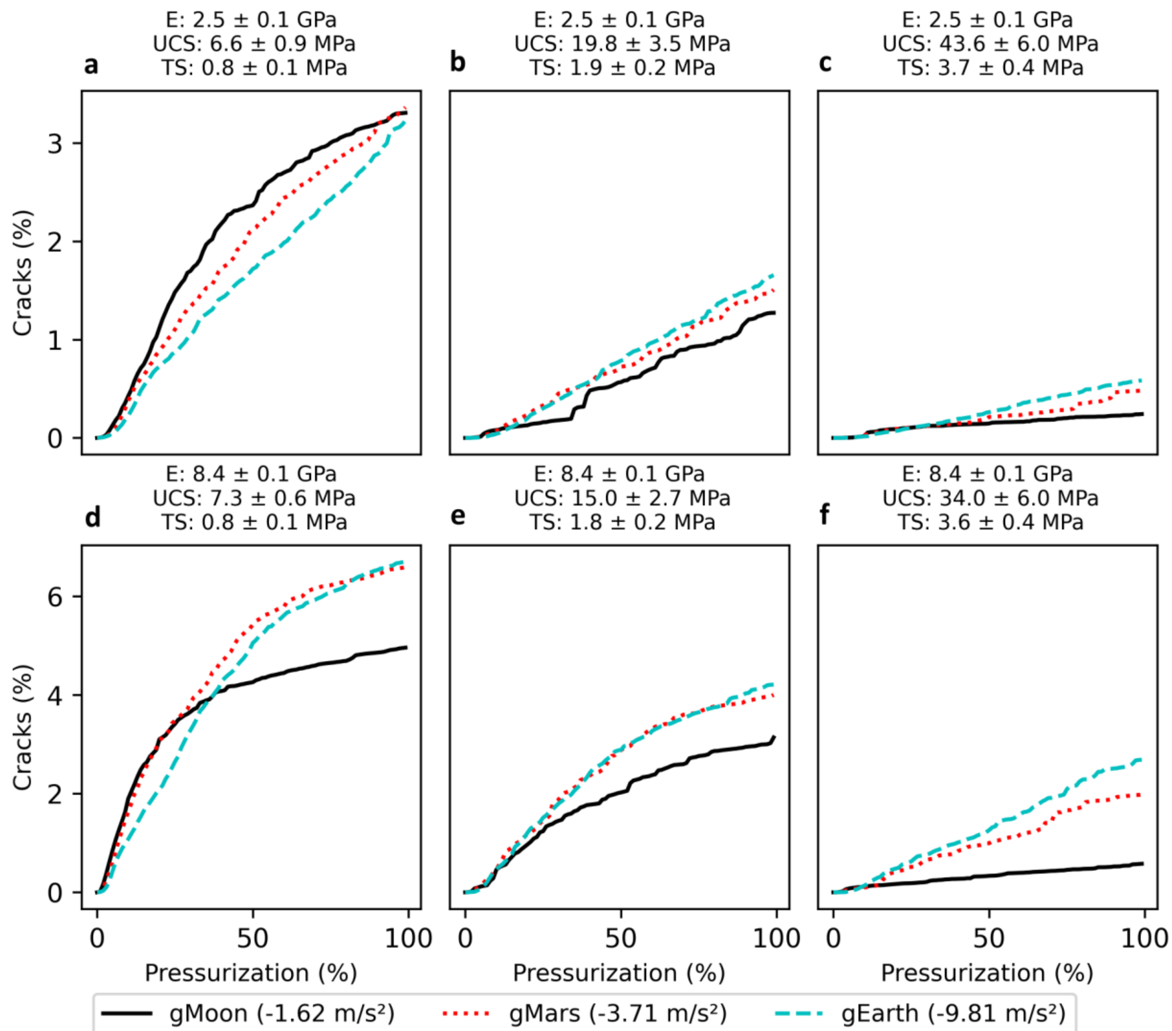

Fig. 6 *Development of cracks (failed particle bonds) during the inflation of the magma body area in 2D DEM simulations subjected to gravity specific to the Moon, Mars, or Earth for a range of host rock Young´s moduli (E), unconfined compressive strengths (UCS) and tensile strengths (TS).*

4 Discussion

Our 18 2D DEM simulations show that the spatial patterns of laccolith-induced deformation vary along a spectrum (Table 1). This spectrum spans the two end-member patterns found by Morand et al. (2024) for similar laccolith inflation volumes and depths.

Morand et al. (2024) attributed this spectrum to differences in the host rock toughness and stiffness, and laccolith depth. Their type 1 end-member includes extensive cracking and high-angle wide shear zones. At the surface, multiple tensile fractures open, and a lower magnitude of surface uplift occurs over a wider area. End-member 1 is more common in stiff rocks with a low toughness above shallower laccoliths. Their type 2 end-member includes limited cracking and low-angle narrow shear zones. At the surface, one central tensile fracture opens, and a higher magnitude of surface uplift occurs over a less extensive area. End-member 2 is more common in tough rocks with a low stiffness above deeper laccoliths. Meng & Hodgetts (2020) found a higher magnitude of surface displacement in stiffer rocks, but their analysis remained qualitative and excludes direct comparison with the crack patterns, (surface) displacement magnitudes and shear strains quantified by Morand et al. (2024) and our study.

Our results confirm that the end-member spectrum of Morand et al. (2024) is additionally controlled by the differences in gravitational acceleration on the Moon, Mars, and Earth. In our results at lower gravity, the type 1 end-member develops a highly cracked host rock, with multiple tensile fractures that open from the surface downward into the host rock and two inward-dipping shear zones that develop from the laccolith edges towards the surface, where they bound the uplifted surface area as thrust faults (e.g., Fig. 3r, Fig. 5r). The type 2 end-member develops a poorly fractured host rock, with one tensile fracture that opens from the surface downward at the crest of the uplifted surface area, and two inward-dipping to near-horizontal fractures that open from the intrusion edges outward (e.g.; Fig. 3p, Fig. 5p). For our toughest rock (TS ~3.7 MPa), the deformation pattern approaches type 1 for higher gravity on Earth and Mars, and type 2 for the Moon´s lower gravity (Fig. 3p-r, Fig. 5p-r). For less tough rock (TS < 2.0 MPa), the highest vertical displacements are generated in a highly fractured type 1 pattern, especially for the Moon´s lower gravity.

Standard models that invert the surface displacements to obtain the diameter, depth and opening of sills and laccoliths, simplify the crustal response to that of a homogeneous, linearly-elastic half-space (Battaglia et al., 2013; Mogi, 1958; Okada, 1985). Those analytical solutions do not involve a gravitational constant, whereas our model results demonstrate a significant effect of gravity on the surface displacements. More recent analytical and finite element models do include a gravitational constant (Fernández et al., 1997; Galland & Scheibert, 2013; Got et al., 2019; Michaut, 2011). At a crustal Young´s modulus of 10 GPa similar to that in our stiffer models, Michaut (2011) finds more displacement over a wider area above laccoliths on the Moon compared to Earth. The slope of the domed surface in their simulations for lunar gravity is overall more gentle compared to the steep-sided and discontinuous pattern in our models. (Wohler & Lena 2009).

Our model results show that syn-intrusive fracturing dynamics instead concentrates shear strain and cracking in narrow zones in the Moon´s crust and delimits the extent of the displaced surface (Fig. 5). The outer shear strain and fracture zones that truncate the surface as reverse faults in the type 1 end-member, impose a lateral constraint on the extent of the surface displacement. The lower gravity on the Moon and Mars reduces the amount of cracking and the magma-induced stress is rather accommodated by upwards crustal displacement in coherent zones that are separated by one or more tensile fractures that propagate from the surface downward. As a result, we observe more vertical surface uplift over a narrower area on the Moon, compared to Earth, with Mars intermediate between the two. Our model results show that the type 1 end-member prevails in rocks with a lower toughness. The weakening effect of the lower porosity of the lunar and Martian crust (Heap et al., 2017), suggests that the type 1 end-member thus should be more common on rocky planetary bodies with a gravity lower than Earth´s. Dynamic fracturing complicates the direct relationship between the extent of the displaced surface (intrusive dome diameter) and the laccolith width and thickness proposed by linearly-elastic models (Michaut et al., 2011; Galland & Scheibert, 2013). Direct comparisons between existing models and our DEM model, using the same strength properties, are now required to determine the uncertainties on existing relationships between the extent and height of lunar and Martian intrusive domes and the dimensions and depth of their underlying intrusions.

Only our models for Earth´s gravity show a central graben, a less uplifted area at the crest of the domed surface that is delimited by normal faults (Figs. 3, 4). The subsurface crack distribution is much more distributed in these conditions compared to those at lower gravities (Fig. 5). Our models for Mars or the Moon show no grabens. Geological observations at exposed igneous plumbing systems, seismic reflection data, and recent volcanic events on Earth, have shown that such graben systems can form as elongated topographic depressions above vertical, magma-filled fractures (dykes) (Magee & Jackson, 2021; Mastin & Pollard, 1988; Sigmundsson et al., 2014; Smittarello et al., 2022). Existing analytical models have used the geometry of such grabens observed on orbital imagery of the Moon or Mars to postulate that the lower gravity there would favor wider opening of higher dykes (Ernst et al., 2001; Head & Wilson, 1993; Klimczak, 2014). The height and opening of those tensile fractures in the crust of Mars or the Moon, versus those on Earth, is not well constrained though (Klimczak, 2015). Tensile fractures in our simulations open wider and propagate deeper from the surface downward on the Moon, and to a lesser extent on Mars, than they can on Earth, for similar amounts of laccolith inflation (Fig. 3, Fig. 5). This progressive fracturing mechanism was not simulated previously, but the favoring of deeper open fractures deeper into the crust on the Moon, in combination with impact-induced surface unloading (Michaut & Pinel, 2018; Wöhler & Lena, 2009), may have favored the ascent of dense mafic magma to the surface there, despite a negative buoyancy contrast with the porous shallow lunar crust.

Our new 2D DEM implementation will allow future simulations to investigate the interaction between extensional crustal stresses and impact-induced unloading, and laccolith-induced stresses. Simulations of broad ranges of laccolith thickness and width are also necessary to investigate if our conclusions hold for the widths of tens of kilometers of intrusive domes and floor-fractured craters found on the Moon and Mars.

Our simulations do not account for the effects of magma viscosity and cooling on flow dynamics and geometric development of laccoliths found previously (Burchardt et al., 2019; Mattsson et al., 2018; Michaut, 2011; Thorey & Michaut, 2016). To investigate such effects on the dynamics of host rock fracturing and displacements will require a different approach for simulating magma flow and laccolith growth that goes beyond this work and that of Morand et al. (2024). Constraints on the porosity, and thus strength, of the lunar and martian crust, remain a source of uncertainty, however, because they are either theoretical, or based on orbital observations, modeling of limited planetary seismic data, or laboratory experiments on terrestrial rocks (Heap et al., 2017; Q. Huang & Wieczorek, 2012; Knapmeyer-Endrun et al., 2021; Wieczorek et al., 2022). Our approach of including a wide range of rock toughnesses and stiffnesses remains necessary, therefore, in numerical simulations of tectonic and magma-induced deformation at gravity lower than Earth´s.

Finally, our DEM models pioneer the direct simulation of dynamic fracturing and high strains induced by inflating laccoliths under different gravitational accelerations, but only in 2D. Three-dimensional DEM simulations of caldera and sinkhole collapse have shown how asymmetrical and anisotropic stresses and fracture patterns can develop (Hardy, 2021; Wang et al., 2022). This limits the interpretation of fracture patterns and displacement patterns observed from orbit on the Moon and Mars. Future 3D DEM modeling will be required to better understand the development of asymmetric surface doming (Lena et al., 2013), hierarchical crack patterns at floor-fractured craters (Montigny et al., 2022), and the accuracy of using elastic rheology theory to infer intrusion depth from observed surface fracture patterns (Walwer et al., 2021).

5 Conclusions

We ran new 2D DEM simulations of displacement, straining, and fracturing of planetary crust by inflating a laccolith at 1.5 kilometer depth. Our simulations show that the different gravitational acceleration on the Moon, Mars, and Earth generates different patterns of laccolith-induced displacements, shear strains and cracking in the subsurface. The same amount of laccolith inflation at the same depth in the lunar or Martian crust induces higher vertical surface displacement in a narrower area compared to what is expected on Earth. This influence of gravitational acceleration impacts estimates of volumes of magma intruded into the shallowest few kilometers of crust on the Moon and Mars. The amount of laccolith-induced cracking is, however, more dominantly controlled by the stiffness and toughness of the planetary crust, as found previously for Earth (Morand et al., 2024). Our model results show that the relation between surface displacements and laccolith dimension and depth in the often already fractured and heterogeneous crusts of planetary bodies is not as direct as suggested by previous models. These findings call for caution regarding existing laccolith inflation model results that assume simplified crustal rheologies or overall ignore different gravities specific to rocky planetary bodies beyond Earth.

Acknowledgments

S.P., A.C., and A.M. received funding from the Norwegian Financial Mechanism 2014–2021 (project “DeMo-Planet” 2020/37/K/ST10/02447) through the Polish National Science Centre (NCN Poland). S.P. acknowledges a postdoctoral ULAM scholarship for 2021-2023 from the Polish National Agency for Academic Exchange (NAWA) and an internal grant for 2024 from the Space Research Centre of the Polish Academy of Sciences (SRC PAS/CBK PAN). This work was initiated during the Erasmus+ exchange of A.C. in 2023, supported by internal funding from SRC PAS. Since 2024, A.M. received funding from the European Research Council (ERC) under the European Union's Horizon 2020 research and innovation program (MAST; grant agreement No. 101003173). C.E.H. provided original scripts in PFC2D which we adapted to simulate laccolith inflation. Itasca Ltd. provided a discounted academic license of their commercial PFC2D software. Discussions with D. Mège, W. Kofman, M.J. Heap, M. Petronis, M. Awdankiewicz, C. Michaut helped improve our work.

Open Research

The authors declare no conflicts of interest relevant to this study. The simulations were produced under an academic license in the commercial software PFC2D (Itasca Ltd.) of which the code cannot be shared publicly. Python scripts used to plot the figures and process the simulation output, as well as the simulation output itself such as particles' positions, displacements, stresses, finite shear strain, radius and group of particles, and cracks' positions, orientations, length and aperture, will be made available in ASCII (.txt) format in a Zenodo data set (Poppe et al., 2024, https://doi.org/10.5281/zenodo.14527262).

References

Bamberg, M., Jaumann, R., Asche, H., Kneissl, T., & Michael, G. G. (2014). Floor-fractured craters on mars - Observations and origin. *Planetary and Space Science*, *98*, 146–162. https://doi.org/10.1016/j.pss.2013.09.017

Battaglia, M., Cervelli, P. F., & Murray, J. R. (2013). Modeling crustal deformation near active faults and volcanic centers-a catalog of deformation models. *US Geological Survey Techniques and Methods, Book 13*, 96. Retrieved from http://pubs.usgs.gov/tm/13/b1/

Brož, P., Hauber, E., Platz, T., & Balme, M. (2015). Evidence for Amazonian highly viscous lavas in the southern highlands on Mars. *Earth and Planetary Science Letters*, *415*, 200–212. https://doi.org/10.1016/j.epsl.2015.01.033

Bunger, A. P., & Cruden, A. R. (2011). Modeling the growth of laccoliths and large mafic sills: Role of magma body forces. *Journal of Geophysical Research: Solid Earth*, *116*(2), 1–18. https://doi.org/10.1029/2010JB007648

Burchardt, S., Mattsson, T., Palma, J. O., Galland, O., Almqvist, B., Mair, K., et al. (2019). Progressive Growth of the Cerro Bayo Cryptodome, Chachahuén Volcano, Argentina—Implications for Viscous Magma Emplacement. *Journal of Geophysical Research: Solid Earth*, *124*(8), 7934–7961. https://doi.org/10.1029/2019JB017543

Carrier, A., Got, J.-L., Peltier, A., Ferrazzini, V., Staudacher, T., Kowalski, P., & Boissier, P. (2015). A damage model for volcanic edifices: Implications for edifice strength, magma pressure, and eruptive processes. *Journal of Geophysical Research: Solid Earth, 120(1)*, 567–583. https://doi.org/10.1002/2014JB011485

Castro, J. M., Cordonnier, B., Schipper, C. I., Tuffen, H., Baumann, T. S., & Feisel, Y. (2016). Rapid laccolith intrusion driven by explosive volcanic eruption. *Nature Communications*, *7*, 13585. https://doi.org/10.1038/ncomms13585

Cundall, P. A., & Strack, O. D. L. (1979). A discrete numerical model for granular assemblies. *Géotechnique*, *29*(1), 47–65. https://doi.org/10.1680/geot.1979.29.1.47

Currier, R. M., & Marsh, B. D. (2015). Mapping real time growth of experimental laccoliths: The effect of solidification on the mechanics of magmatic intrusion. *Journal of Volcanology and Geothermal Research*, *302*, 211–224. https://doi.org/10.1016/j.jvolgeores.2015.07.009

Daniels, K. A., Kavanagh, J., Menand, T., Sparks, R. S. J., Daniels, K. A., Kavanagh, J., et al. (2012). The shapes of dikes : Evidence for the influence of cooling and inelastic deformation. *Geological Society of America Bulletin*, *124*(7/8), 1102–1112.

Ernst, R. E., Grosfils, E. B., & Mège, D. (2001). Giant dike swarms: Earth, Venus, and Mars. *Annual Reviews in Earth and Planetary Science*, *29*, 489–534. https://doi.org/10.1146/annurev.earth.29.1.489

Farrand, W. H., Lane, M. D., Edwards, B. R., & Aileen Yingst, R. (2011). Spectral evidence of volcanic cryptodomes on the northern plains of Mars. *Icarus*, *211*(1), 139–156. https://doi.org/10.1016/j.icarus.2010.09.006

Farrand, W. H., Rice, J. W., Chuang, F. C., & Rogers, A. D. (2021). Spectral and geological analyses of domes in western Arcadia Planitia, Mars: Evidence for intrusive alkali-rich volcanism and ice-associated surface features. *Icarus*, *357*. https://doi.org/10.1016/j.icarus.2020.114111

Fernández, J., Rundle, J. B., Granell, R. D. R., & Yu, T.-T. (1997). Programs to compute deformation due to a magma intrusion in elastic-gravitational layered Earth models. *Computers & Geosciences*, *23*(3), 231–249. https://doi.org/10.1016/S0098-3004(96)00066-0

Galland, O., & Scheibert, J. (2013). Analytical model of surface uplift above axisymmetric flat-lying magma intrusions: Implications for sill emplacement and geodesy. *Journal of Volcanology and Geothermal Research*, *253*, 114–130. https://doi.org/10.1016/j.jvolgeores.2012.12.006

Galland, O., Holohan, E. P., van Wyk de Vries, B., & Burchardt, S. (2018). Laboratory Modelling of Volcano Plumbing Systems: A Review. In C. Breitkreuz & S. Rocchi (Eds.), *Physical Geology of Shallow Magmatic Systems - Dykes, Sills and Laccoliths* (pp. 147–214). Springer Berlin Heidelberg.

Gilbert, G. K. (1877). *Geology of the Henry Mountains*. Washington, D.C.

Gerbault, M., Hassani, R., Novoa Lizama, C., & Souche, A. (2018). Three-dimensional failure patterns around an inflating magmatic chamber. *Geochemistry, Geophysics, Geosystems, 19(3)*, 749–771. https://doi.org/10.1002/2017GC007174

Got, J. L., Amitrano, D., Stefanou, I., Brothelande, E., & Peltier, A. (2019). Damage and Strain Localization Around a Pressurized Shallow-Level Magma Reservoir. *Journal of Geophysical Research: Solid Earth*, *124*(2), 1443–1458. https://doi.org/10.1029/2018JB016407

Grosfils, E. B., Mcgovern, P. J., Gregg, P. M., Galgana, G. A., Hurwitz, D. M., Long, S. M., & Chestler, S. R. (2015). Elastic models of magma reservoir mechanics: A key tool for

investigating planetary volcanism. *Geological Society Special Publication*, *401*, 239–267. https://doi.org/10.1144/SP401.2
Hall, J. L., & Solomon, S. C. (1981). Lunar Floor-Fractured Craters: Evidence for Viscous Relaxation of Crater Topography. *Journal of Geophysical Research*, *86*(B10), 9537–9552.
Hardy, S. (2021). Discrete element modelling of pit crater formation on mars. *Geosciences (Switzerland)*, *11*(7). https://doi.org/10.3390/geosciences11070268
Harnett, C. E., Heap, M. J., & Thomas, M. E. (2020). A toolbox for identifying the expression of dome-forming volcanism on exoplanets. *Planetary and Space Science*, *180*, 104762. https://doi.org/10.1016/j.pss.2019.104762
Harnett, C. E., Benson, P. M., Rowley, P., & Fazio, M. (2018). Fracture and damage localization in volcanic edifice rocks from El Hierro, Stromboli and Tenerife. *Scientific Reports*, *8*(1). https://doi.org/10.1038/s41598-018-20442-w
Harnett, C. E., & Heap, M. J. (2021). Mechanical and topographic factors influencing lava dome growth and collapse. *Journal of Volcanology and Geothermal Research*, *420*, 107398. https://doi.org/10.1016/j.jvolgeores.2021.107398
Harnett, C.E., Watson, R.A., Holohan, E.P., & Schöpfer, M.P. (2023). Collapse caldera walls: Mechanical controls on slope failure and morphology. *Journal of Volcanology and Geothermal Research*, *442*, 107893. https://doi.org/10.1016/j.jvolgeores.2023.107893
Haug, O., Galland, O., Souloumiac, P., Souche, A., Guldstrand, F., & Schmiedel, T. (2017). Inelastic damage as a mechanical precursor for the emplacement of saucer-shaped intrusions. *Geology, 45(12)*, 1099–1102. https://doi.org/10.1130/G39361.1
Head, J. W., & Wilson, L. (1993). Lunar graben formation due to near-surface deformation accompanying dike emplacement Introduction and background. *Planetary and Space Science,* 41.
Head, J. W., & Wilson, L. (2017). Generation, ascent and eruption of magma on the Moon: New insights into source depths, magma supply, intrusions and effusive/explosive eruptions (Part 2: Predicted emplacement processes and observations). *Icarus*, *283*, 176–223. https://doi.org/10.1016/j.icarus.2016.05.031
Heap, M. J., Byrne, P. K., & Mikhail, S. (2017). Low surface gravitational acceleration of Mars results in a thick and weak lithosphere : Implications for topography, volcanism, and hydrology. *Icarus*, *281*, 103–114. https://doi.org/10.1016/j.icarus.2016.09.003
Heap, M. J., Villeneuve, M., Albino, F., Farquharson, J. I., Brothelande, E., Amelung, F., et al. (2020). Towards more realistic values of elastic moduli for volcano modelling. *Journal of Volcanology and Geothermal Research*, *390*, 106684. https://doi.org/10.1016/j.jvolgeores.2019.106684
Heap, M. J., Wadsworth, F. B., Heng, Z., Xu, T., Griffiths, L., Aguilar Velasco, A., et al. (2021). The tensile strength of volcanic rocks: Experiments and models. *Journal of Volcanology and Geothermal Research*, *418*, 107348. https://doi.org/10.1016/j.jvolgeores.2021.107348
Holohan, E. P., Schöpfer, M. P. J., & Walsh, J. J. (2011). Mechanical and geometric controls on the structural evolution of pit crater and caldera subsidence. *Journal of*

Geophysical Research: Solid Earth, *116*(7), 1–23. https://doi.org/10.1029/2010JB008032
Holohan, E. P., Schöpfer, M. P. J., & Walsh, J. J. (2015). Stress evolution during caldera collapse. *Earth and Planetary Science Letters*, *421*, 139–151. https://doi.org/10.1016/j.epsl.2015.03.003
Huang, L., Dontsov, E., Fu, H., Lei, Y., Weng, D., & Zhang, F. (2022). Hydraulic fracture height growth in layered rocks: Perspective from DEM simulation of different propagation regimes. *International Journal of Solids and Structures*, *238*, 111395. https://doi.org/10.1016/j.ijsolstr.2021.111395
Huang, Q., & Wieczorek, M. A. (2012). Density and porosity of the lunar crust from gravity and topography. *Journal of Geophysical Research: Planets*, *117*(5), E05003. https://doi.org/10.1029/2012JE004062
Ivanov, M. A., Head, J. W., & Bystrov, A. (2016). The lunar Gruithuisen silicic extrusive domes: Topographic configuration, morphology, ages, and internal structure. *Icarus*, *273*, 262–283. https://doi.org/10.1016/j.icarus.2015.12.015
Jaeger, J. C., Cook, N. G. W., & Zimmerman, R. W. (2007). *Fundamentals of Rock Mechanics*. *Cambridge University Press* (Vol. 1). https://doi.org/10.1017/CBO9781107415324.004
Jiang, M., Shen, Z., & Wang, J. (2015). A novel three-dimensional contact model for granulates incorporating rolling and twisting resistances. *Computers and Geotechnics*, *65*, 147–163. https://doi.org/10.1016/j.compgeo.2014.12.011
Jozwiak, L. M., Head, J. W., Zuber, M. T., Smith, D. E., & Neumann, G. A. (2012). Lunar floor-fractured craters: Classification, distribution, origin and implications for magmatism and shallow crustal structure. *Journal of Geophysical Research: Planets*, *117*(11), 1–23. https://doi.org/10.1029/2012JE004134
Kavanagh, J. L., Burns, A. J., Hilmi Hazim, S., Wood, E. P., Martin, S. A., Hignett, S., & Dennis, D. J. C. (2018). Challenging dyke ascent models using novel laboratory experiments: Implications for reinterpreting evidence of magma ascent and volcanism. *Journal of Volcanology and Geothermal Research*, *354*, 87–101. https://doi.org/10.1016/j.jvolgeores.2018.01.002
Klimczak, C. (2014). Geomorphology of lunar grabens requires igneous dikes at depth. *Geology*, *42*(11), 963–966. https://doi.org/10.1130/G35984.1
Klimczak, C. (2015). Limits on the brittle strength of planetary lithospheres undergoing global contraction. *Journal of Geophysical Research: Planets*, *120*(12), 2135–2151. https://doi.org/10.1002/2015JE004851
Knapmeyer-Endrun, B., Panning, M., Bissig, F., Joshi, R., Khan, A., Kim, D., et al. (2021). Thickness and structure of the Martian crust from InSight seismic data. *Advancement of Science*, *373*(6553), 438–443. https://doi.org/10.1126/science.abf8966ï
Lena, R., Wöhler, C., Phillips, J., & Chiocchetta, M. T. (2013). *Lunar Domes*. Milano: Springer Milan. https://doi.org/10.1007/978-88-470-2637-7
Ma, Y., & Huang, H. (2018a). A displacement-softening contact model for discrete element modeling of quasi-brittle materials. *International Journal of Rock Mechanics and Mining Sciences*, *104*, 9–19. https://doi.org/10.1016/j.ijrmms.2018.02.007

Ma, Y., & Huang, H. (2018b). DEM analysis of failure mechanisms in the intact Brazilian test. *International Journal of Rock Mechanics and Mining Sciences*, *102*(November 2017), 109–119. https://doi.org/10.1016/j.ijrmms.2017.11.010

Magee, C., & Jackson, C. A.-L. (2021). Can we relate the surface expression of dike-induced normal faults to subsurface dike geometry? *Geology*, *49*(4), 366–371. https://doi.org/https://doi.org/10.1130/G48171.1

Magee, C., Stevenson, C. T. E., Ebmeier, S. K., Keir, D., Hammond, J. O. S., Gottsmann, J. H., et al. (2018). Magma Plumbing Systems: A Geophysical Perspective. *Journal of Petrology*, (June), 1–35. https://doi.org/10.1093/petrology/egy064

Mastin, L. G., & Pollard, D. D. (1988). Surface deformation and shallow dike intrusion processes at Inyo Craters, Long Valley, California. *Journal of Geophysical Research*, *93*(B11), 13221–13235. https://doi.org/10.1029/JB093iB11p13221

Mattsson, T., Burchardt, S., Almqvist, B. S. G., & Ronchin, E. (2018). Syn-emplacement fracturing in the sandfell laccolith, eastern iceland—implications for rhyolite intrusion growth and volcanic hazards. *Frontiers in Earth Science*, *6:5*. https://doi.org/10.3389/feart.2018.00005

McGovern, P. J., Grosfils, E. B., Galgana, G. A., Morgan, J. K., Rumpf, M. E., Smith, J. R., & Zimbelman, J. R. (2014). Lithospheric flexure and volcano basal boundary conditions; keys to the structural evolution of large volcanic edifices on the terrestrial planets. *Geological Society, London, Special Publications,* 401, 219-237. https://doi.org/doi:10.1144/SP401.7

Michaut, C. (2011). Dynamics of magmatic intrusions in the upper crust: Theory and applications to laccoliths on Earth and the Moon. *Journal of Geophysical Research*, *116*(B5). https://doi.org/10.1029/2010jb008108

Michaut, C., Baratoux, D., & Thorey, C. (2013). Magmatic intrusions and deglaciation at mid-latitude in the northern plains of Mars. *Icarus*, *225*(1), 602–613. https://doi.org/10.1016/j.icarus.2013.04.015

Michaut, C., & Pinel, V. (2018). Magma Ascent and Eruption Triggered by Cratering on the Moon. *Geophysical Research Letters*, *45*(13), 6408–6416. https://doi.org/10.1029/2018GL078150

Michaut, C., Pinel, V., & Maccaferri, F. (2020). Magma ascent at floor-fractured craters diagnoses the lithospheric stress state on the Moon. *Earth and Planetary Science Letters*, *530*, 115889. https://doi.org/10.1016/j.epsl.2019.115889

Mogi, K. (1958). Relations between the eruptions of various volcanoes and the deformations of the ground surfaces around them. *Bulletin of the Earthquake Research Institute*. https://doi.org/10.1016/j.epsl.2004.04.016

Montanari, D., Bonini, M., Corti, G., Agostini, A., & Del Ventisette, C. (2017). Forced folding above shallow magma intrusions: Insights on supercritical fluid flow from analogue modelling. *Journal of Volcanology and Geothermal Research*, *345*, 67–80. https://doi.org/10.1016/j.jvolgeores.2017.07.022

Montigny, A., Walwer, D., & Michaut, C. (2022). The origin of hierarchical cracks in floor-fractured craters on Mars and the Moon. *Earth and Planetary Science Letters*, *600*, 117887. https://doi.org/10.1016/j.epsl.2022.117887

Morand, A., Poppe, S., Harnett, C., Cornillon, A., Heap, M., & Mège, D. (2024). Fracturing and Dome-Shaped Surface Displacements Above Laccolith Intrusions: Insights From Discrete Element Method Modeling. *Journal of Geophysical Research: Solid Earth*, *129*(3), e2023JB027423. https://doi.org/10.1029/2023JB027423

Morgan, J. K., & McGovern, P. J. (2005). Discrete element simulations of gravitational volcanic deformation: 1. Deformation structures and geometries. *Journal of Geophysical Research: Solid Earth*, *110*(5), 1–22. https://doi.org/10.1029/2004JB003252

Morgan, S. (2018). Pascal's Principle, a Simple Model to Explain the Emplacement of Laccoliths and Some Mid-crustal Plutons. *Volcanic and Igneous Plumbing Systems*, 139–165. https://doi.org/10.1016/B978-0-12-809749-6.00006-6

Okada, Y. (1985). Surface deformation due to shear and tensile faults in a half space. *Bulletin of the Seismological Society of America*, *75*(4), 1135–1154.

Petronis, M. S., van Wyk de Vries, B., & Garza, D. (2019). The leaning Puy de Dôme (Auvergne, France) tilted by shallow intrusions. *Volcanica*, *2*(2), 161–189. https://doi.org/10.30909/vol.02.02.161186

Platz, T., Byrne, P. K., Massironi, M., & Hiesinger, H. (2015). Volcanism and tectonism across the inner solar system: An overview. *Geological Society Special Publication*, *401*, 1–56. https://doi.org/10.1144/SP401.22

Pollard, D. D. (1973). Derivation and evaluation of a mechanical model for sheet intrusions. *Tectonophysics*, *19*(3), 233–269. https://doi.org/10.1016/0040-1951(73)90021-8

Pollard, D. D., & Johnson, A. M. (1973). Mechanics of growth of some laccolithic intrusions in the Henry Mountains, Utah, II: bending and failure of overburden layers and sill formation. *Tectonophysics*, *18*(3–4), 311–354. https://doi.org/10.1016/0040-1951(73)90051-6

Poppe, S., Holohan, E. P., Galland, O., Buls, N., Van Gompel, G., Keelson, B., et al. (2019). An Inside Perspective on Magma Intrusion: Quantifying 3D Displacement and Strain in Laboratory Experiments by Dynamic X-Ray Computed Tomography. *Frontiers in Earth Science*, *7*, 62. https://doi.org/10.3389/feart.2019.00062

Poppe, S., Cornillon, A., Morand, A., & Harnett, C. (2024). Discrete Element Method model results of laccolith intrusion inflation on the Moon, Mars, and Earth. *Data set, Zenodo*. https://doi.org/10.5281/zenodo.14527262

Potyondy, D. O., & Cundall, P. A. (2004). A bonded-particle model for rock. *International Journal of Rock Mechanics and Mining Sciences*, *41*(8), 1329–1364. https://doi.org/10.1016/j.ijrmms.2004.09.011

Rampey, M. L., Milam, K. A., McSween, H. Y., Moersch, J. E., & Christensen, P. R. (2007). Identity and emplacement of domical structures in the western Arcadia Planitia, Mars. *Journal of Geophysical Research: Planets*, *112*(6), E06011. https://doi.org/10.1029/2006JE002750

Scheibert, J., Galland, O., & Hafver, A. (2017). Inelastic deformation during sill and laccolith emplacement: Insights from an analytic elastoplastic model. *Journal of Geophysical Research: Solid Earth*, *122*(2), 923–945. https://doi.org/10.1002/2016JB013754

Schmiedel, T., Galland, O., & Breitkreuz, C. (2017). Dynamics of Sill and Laccolith Emplacement in the Brittle Crust: Role of Host Rock Strength and Deformation Mode. *Journal of Geophysical Research: Solid Earth*, *122*(11), 8860–8871. https://doi.org/10.1002/2017JB014468

Schöpfer, M. P. J., Childs, C., & Walsh, J. J. (2006). Localisation of normal faults in multilayer sequences. *Journal of Structural Geology*, *28*(5), 816–833. https://doi.org/10.1016/j.jsg.2006.02.003

Schöpfer, M. P. J., Abe, S., Childs, C., & Walsh, J. J. (2009). The impact of porosity and crack density on the elasticity, strength and friction of cohesive granular materials: Insights from DEM modelling. *International Journal of Rock Mechanics and Mining Sciences*, *46*(2), 250–261. https://doi.org/10.1016/j.ijrmms.2008.03.009

Schöpfer, M.P., & Lehner, F.K. (2024). The rise and fall of diapirs during thin-skinned extension revisited. *Journal of Structural Geology, 188*, 105165. https://doi.org/10.1016/j.jsg.2024.105165

Schultz, P. H. (1976). Floor-fractured lunar craters. *The Moon*, *15*(3–4), 241–273. https://doi.org/10.1007/BF00562240

Segall, P. (2010). Earthquake and volcano deformation. *Princeton University Press*, Princeton, New Yersey. https://doi.org/10.5860/choice.48-0287

Sigmundsson, F., Hooper, A., Hreinsdóttir, S., Vogfjörd, K. S., Ófeigsson, B. G., Heimisson, E. R., et al. (2014). Segmented lateral dyke growth in a rifting event at Bárðarbunga volcanic system, Iceland. *Nature*, *517*(7533), 15. https://doi.org/10.1038/nature14111

Smittarello, D., Smets, B., Barrière, J., Michellier, C., Oth, A., Shreve, T., et al. (2022). Precursor-free eruption triggered by edifice rupture at Nyiragongo volcano. *Nature*, *609*(September). https://doi.org/10.1038/s41586-022-05047-8

Thomas, R. J., Rothery, D. A., Conway, S. J., & Anand, M. (2015). Explosive volcanism in complex impact craters on Mercury and the Moon: Influence of tectonic regime on depth of magmatic intrusion. *Earth and Planetary Science Letters*, *431*, 164–172. https://doi.org/10.1016/j.epsl.2015.09.029

Thorey, C., & Michaut, C. (2014). A model for the dynamics of crater-centered intrusion: Application to lunar floor-fractured craters, *Journal of Geophysical Research: Planets*, *119*, 286-312. https://doi.org/10.1002/2013JE004467

Thorey, C., & Michaut, C. (2016). Elastic-plated gravity currents with a temperature-dependent viscosity. *Journal of Fluid Mechanics, 805*, 88–117. https://doi.org/10.1017/jfm.2016.538

Vaucher, J., Baratoux, D., Mangold, N., Pinet, P., Kurita, K., & Grégoire, M. (2009). The volcanic history of central Elysium Planitia: Implications for martian magmatism. *Icarus*, *204*(2), 418–442. https://doi.org/10.1016/j.icarus.2009.06.032

Villeneuve, M.C., & Heap, M.J. (2021). Calculating the cohesion and internal friction angle of volcanic rocks and rock masses. *Volcanica*, *4*(2), 279-293. https://doi.org/10.30909/vol.04.02.279293

Walwer, D., Michaut, C., Pinel, V., & Adda-Bedia, M. (2021). Magma ascent and emplacement below floor fractured craters on the Moon from floor uplift and fracture length. *Physics of the Earth and Planetary Interiors*, *312*, 106658. https://doi.org/10.1016/j.pepi.2021.106658

Wang, T., Zhang, F., Furtney, J., & Damjanac, B. (2022). A review of methods, applications and limitations for incorporating fluid flow in the discrete element method. *Journal of Rock Mechanics and Geotechnical Engineering*, *14*(3), 1005–1024. https://doi.org/10.1016/j.jrmge.2021.10.015

Wieczorek, M. A., Neumann, G. A., Nimmo, F., Kiefer, W. S., Taylor, G. J., Melosh, H. J., et al. (2013). The crust of the Moon as seen by GRAIL. *Science*, *339*(6120), 671–675. https://doi.org/10.1126/science.1231530

Wieczorek, M. A., Broquet, A., Mclennan, S. M., Rivoldini, A., Golombek, M., Antonangeli, D., et al. (2022). InSight Constraints on the Global Character of the Martian Crust. *Journal of Geophysical Research : Planets, 127:5*, e2022JE007298. https://doi.org/10.1029/2022JE007298

Wilhelms, D. E. (1987). The geologic history of the Moon. *U.S. Geological Survey Professional Paper*, *1348*, 1–293. https://doi.org/10.3133/pp1348

Wilson, P. I. R., McCaffrey, K. J. W., Wilson, R. W., Jarvis, I., & Holdsworth, R. E. (2016). Deformation structures associated with the Trachyte Mesa intrusion, Henry Mountains, Utah: Implications for sill and laccolith emplacement mechanisms. *Journal of Structural Geology*, *87*, 30–46. https://doi.org/10.1016/j.jsg.2016.04.001

Wöhler, C., & Lena, R. (2009). Lunar intrusive domes: Morphometric analysis and laccolith modelling. *Icarus*, *204*(2), 381–398. https://doi.org/10.1016/j.icarus.2009.07.031

Woodell, D. R., Schöpfer, M. P. J., & Holohan, E. P. (2023). Numerical models of restless caldera volcanoes. *Earth and Planetary Science Letters*, *621*, 118376. https://doi.org/10.1016/j.epsl.2023.118376

Supporting Information for

Gravity affects magma-induced crustal deformation: comparing the Moon, Mars, and Earth

S. Poppe[1], A. Cornillon[1,2], A. Morand[1,3], and C. E. Harnett[4]

[1]Centrum Badań Kosmicznych Polskiej Akademi Nauk, Bartycka 18A, 00-716 Warsaw, Poland. [2]Université Paris-Saclay, CNRS, GEOPS, Orsay, France. [3]School of Earth Sciences, Bristol University, United Kingdom. [4]UCD School of Earth Sciences, University College Dublin, Belfield, Dublin 4, Ireland.

Contents of this file

Text S1 and S2
Figures S01 to S19
Table S1

Additional Supporting Information (Files uploaded separately)

Captions for Movies S01 to S18

Introduction

This supporting information contains an additional text (Text S1) which describes the methodology of the numerical rock experiments performed to determine mechanical strength properties of the rock in the main paper in the particle flow code PFC2D (version 7.0; Itasca Consultants GmbH). Figures S01 to S18 display the different components of displacement, stress and crack pattern results, and the derived strain patterns for each performed simulation. Figure S19 illustrates the numerical rock experiments results. Table S1 contains all constant numerical parameters used in the DEM simulations in the main text. This supporting information also contains the captions of the movies which show the temporal evolution of the fracture pattern and the normalized finite shear strain in function of pressurization for all models. The movie files are uploaded separately.

Text S1. Determination of mechanical rock strength properties

To obtain rock mechanical properties we follow the methodology of Harnett and Heap (2021) that is reproduced in Morand et al. (2024). We perform Unconfined

Compressive Strength (UCS) tests to obtain the compressive strength and Young's modulus E of our modeled material. A compressive rate of 10^{-1} m/s^{-1} was applied on a sample of 1 km height by 0.5 km width, which respects the ratio of 1:2 while keeping the same particle size as in the model (radius = 8.66 +/- 1.66 m). Compressive strength corresponds to the maximum stress, and the Young's modulus to the slope of the linear portion of the strain-stress curve. We also performed direct tensile tests at a rate of 10^{-2} m/s^{-1} to obtain the bulk tensile strength of the modeled rock. Tensile strength corresponds to the maximum stress of the strain-stress curve. The determined rock properties are depending on the particle assembly. For each set of particle bond parameter values, we use the average of 15 strength experiments to determine the Young's modulus, compressive and tensile strength. Figure S19 displays the simulated cracks for one example test per particle bond strength, and the stress-strain results for all experiments.

Text S2. Cutoff in Figures S01 to S18

At the surface, some fully detached particles can roll or fall in vertical cracks. Thus, these particles have very high displacement in comparison to other particles. We follow the methodology of Morand et al. (2024) described in their Supporting Information, by looking at the distribution of the values of the vertical and horizontal displacement to set the same cutoff for all simulations. To set the cutoff, we consider the two displacement components for all simulations at 100% of injection. Then, we choose the value that cuts off only 0.5% of all negative displacement and 0.5% of all positive displacement, thus we are representing 99% of all displacements.

Due to large displacement near cracks, some particles have a much higher strain compared to other particles. However, by considering all strain components at 100% of injection for all simulations, at least 90% of the data are comprised in a small range of 0.05%. Thus for all Figures S07 to S18, we applied the same cutoff for the different strain components: the maximum principal strain is cut off between 1.0% and 1.05%, the minimum principal strain is cut off between 0.95% and 1.0% and shear is cut off, as in the main text, between 0.0% and 0.05%. To emphasize the variation, each component is then normalized. Principal stresses are cut off between -150 and 15 MPa.

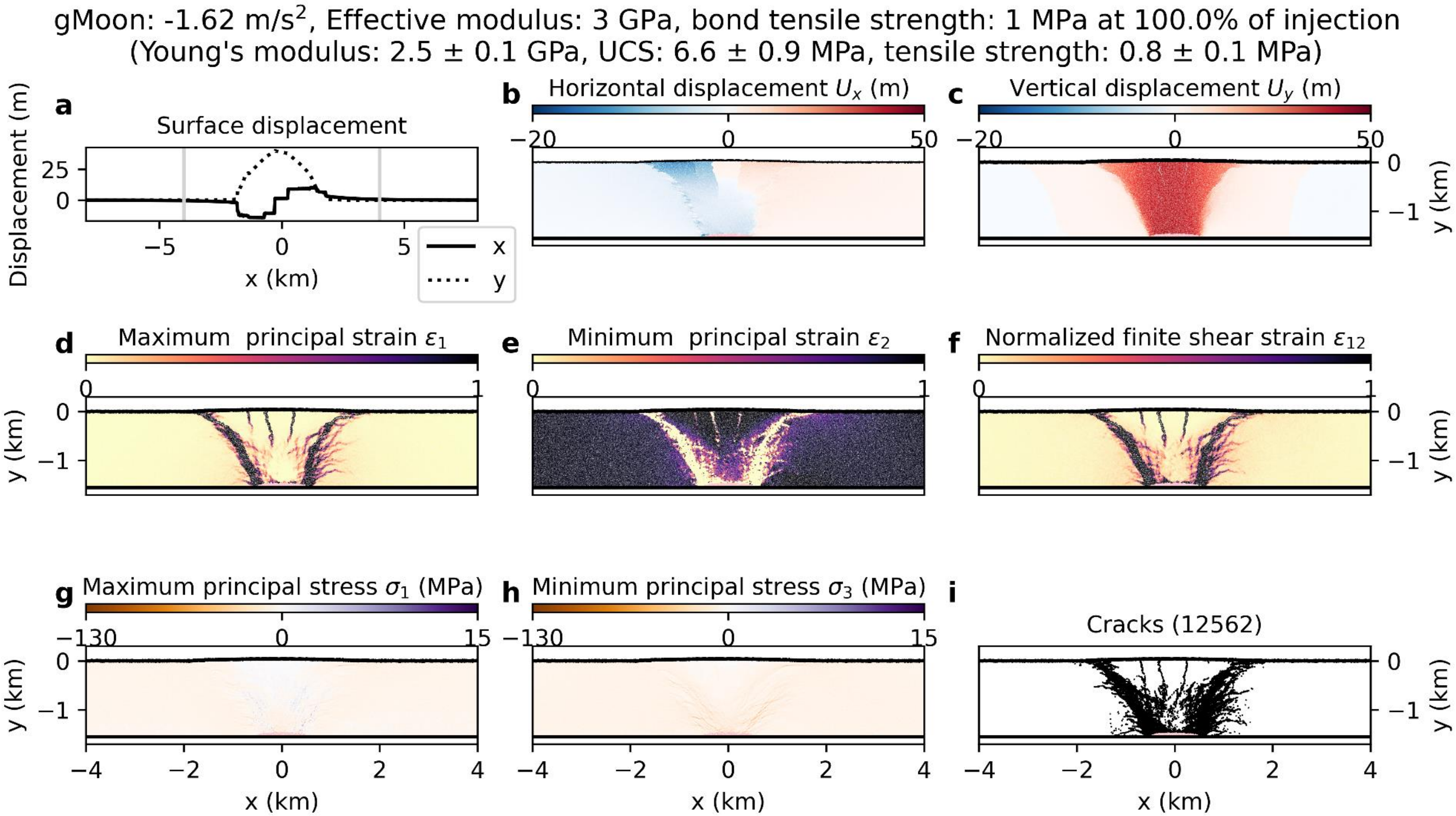

Figure S01. Deformation components at 100% of laccolith pressurization on the Moon: (a) horizontal x and vertical y surface displacement; (b) horizontal displacement; (c) vertical displacement; (d) maximum principal strain; (e) minimum principal strain; (f) normalized finite shear strain; (g) maximum principal stress; (h) minimum principal stress; (i) broken particle bonds (cracks) as black lines. See Text S2 above for details on the cutoff on displacements (b, c), strains (d, e, f), and stresses (g, h).

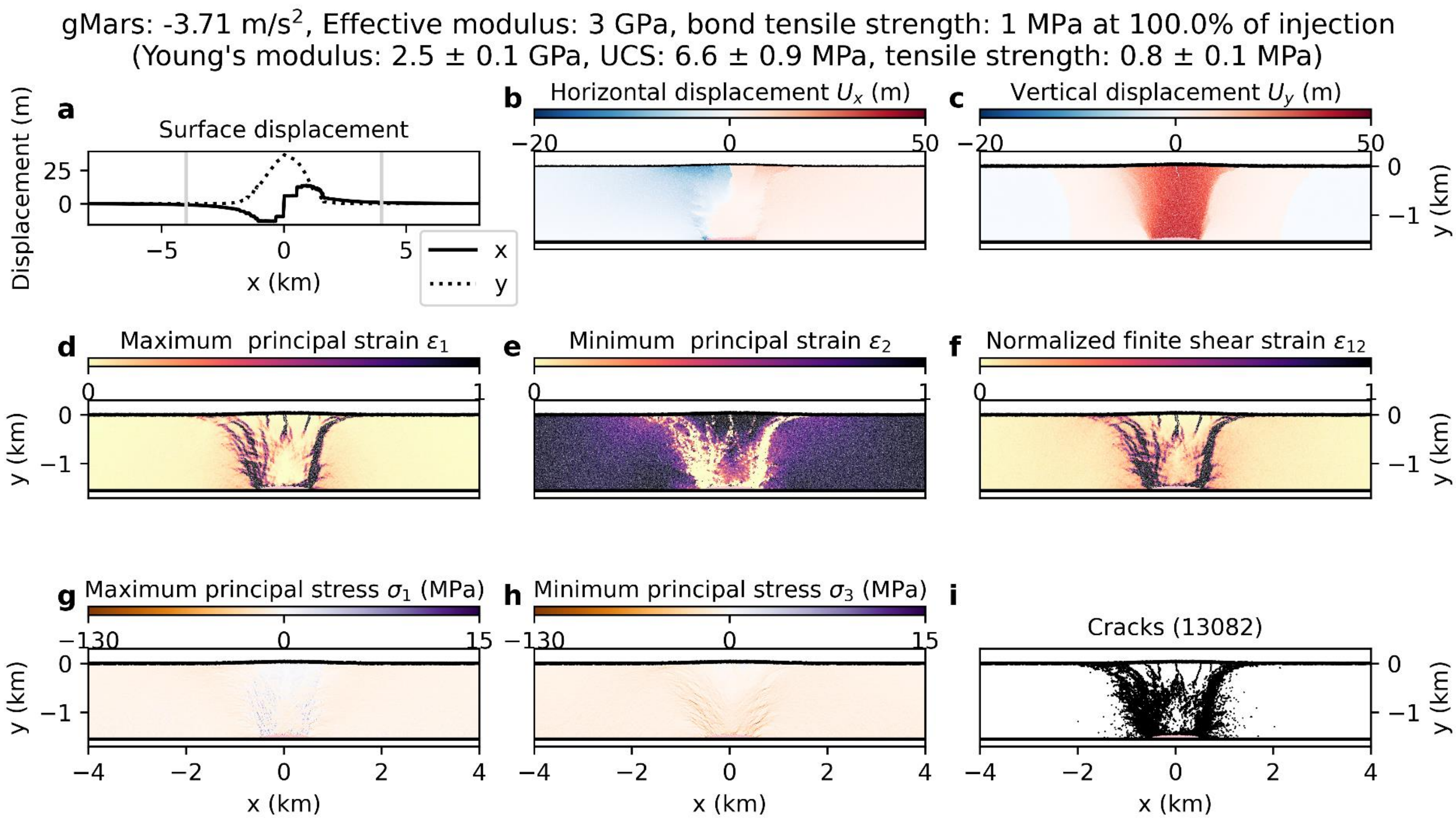

Figure S02. Deformation components at 100% of laccolith pressurization on Mars: (a) horizontal x and vertical y surface displacement; (b) horizontal displacement; (c) vertical displacement; (d) maximum principal strain; (e) minimum principal strain; (f) normalized finite shear strain; (g) maximum principal stress; (h) minimum principal stress; (i) broken particle bonds (cracks) as black lines. See Text S2 above for details on the cutoff on displacements (b, c), strains (d, e, f), and stresses (g, h).

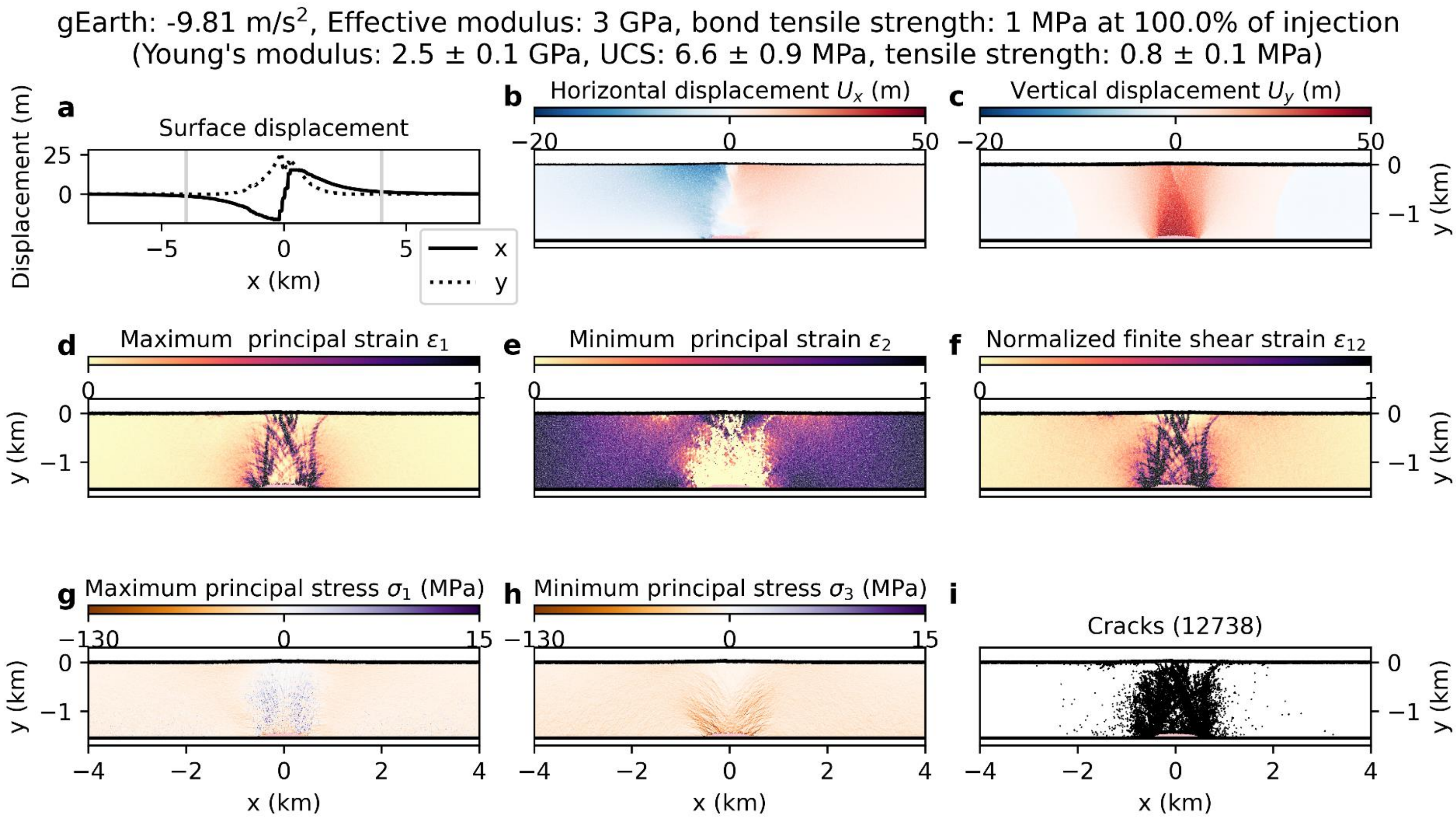

Figure S03. Deformation components at 100% of laccolith pressurization on Earth: (a) horizontal x and vertical y surface displacement; (b) horizontal displacement; (c) vertical displacement; (d) maximum principal strain; (e) minimum principal strain; (f) normalized finite shear strain; (g) maximum principal stress; (h) minimum principal stress; (i) broken particle bonds (cracks) as black lines. See Text S2 above for details on the cutoff on displacements (b, c), strains (d, e, f), and stresses (g, h).

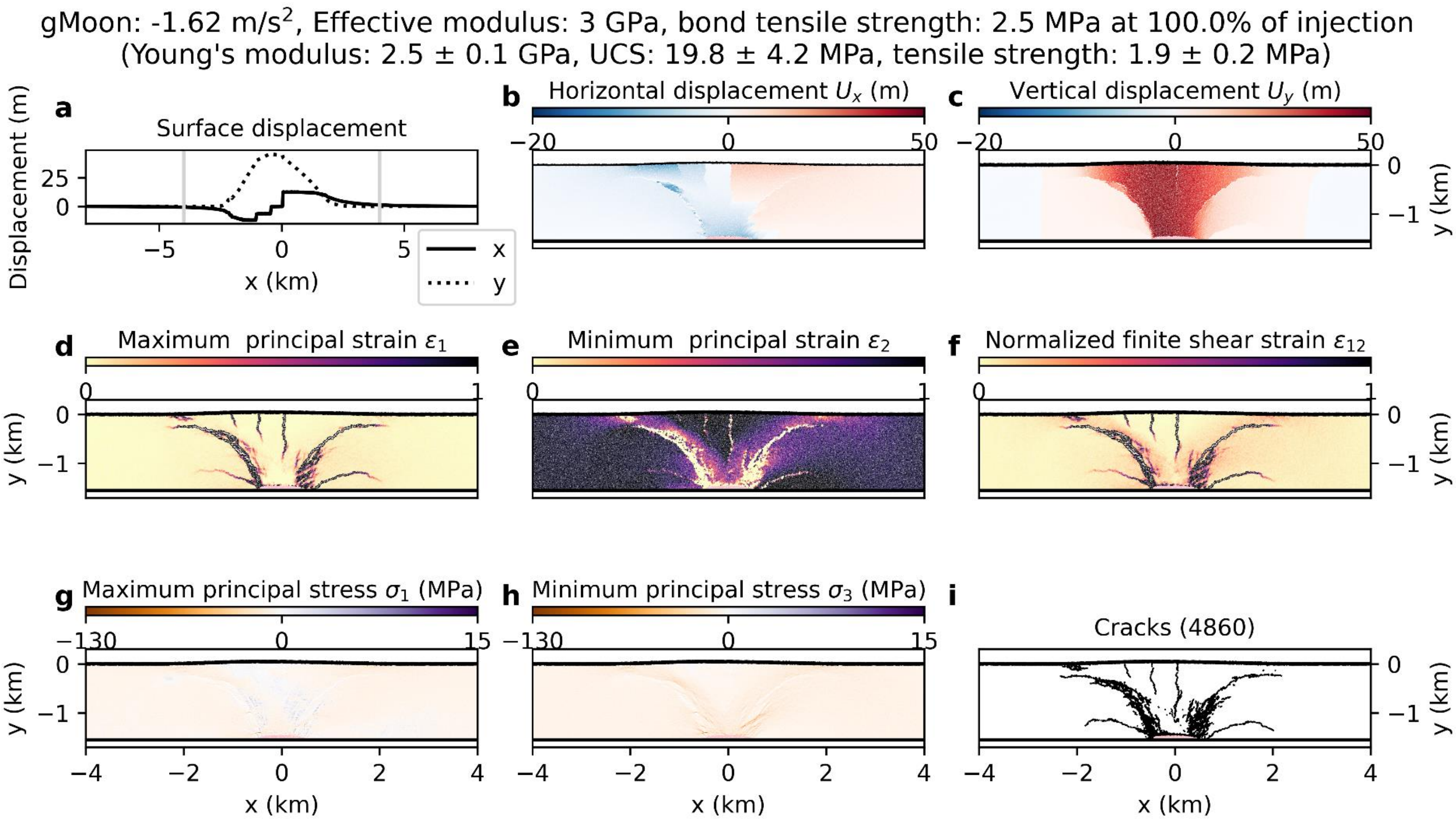

Figure S04. Deformation components at 100% of laccolith pressurization on the Moon: (a) horizontal x and vertical y surface displacement; (b) horizontal displacement; (c) vertical displacement; (d) maximum principal strain; (e) minimum principal strain; (f) normalized finite shear strain; (g) maximum principal stress; (h) minimum principal stress; (i) broken particle bonds (cracks) as black lines. See Text S2 above for details on the cutoff on displacements (b, c), strains (d, e, f), and stresses (g, h).

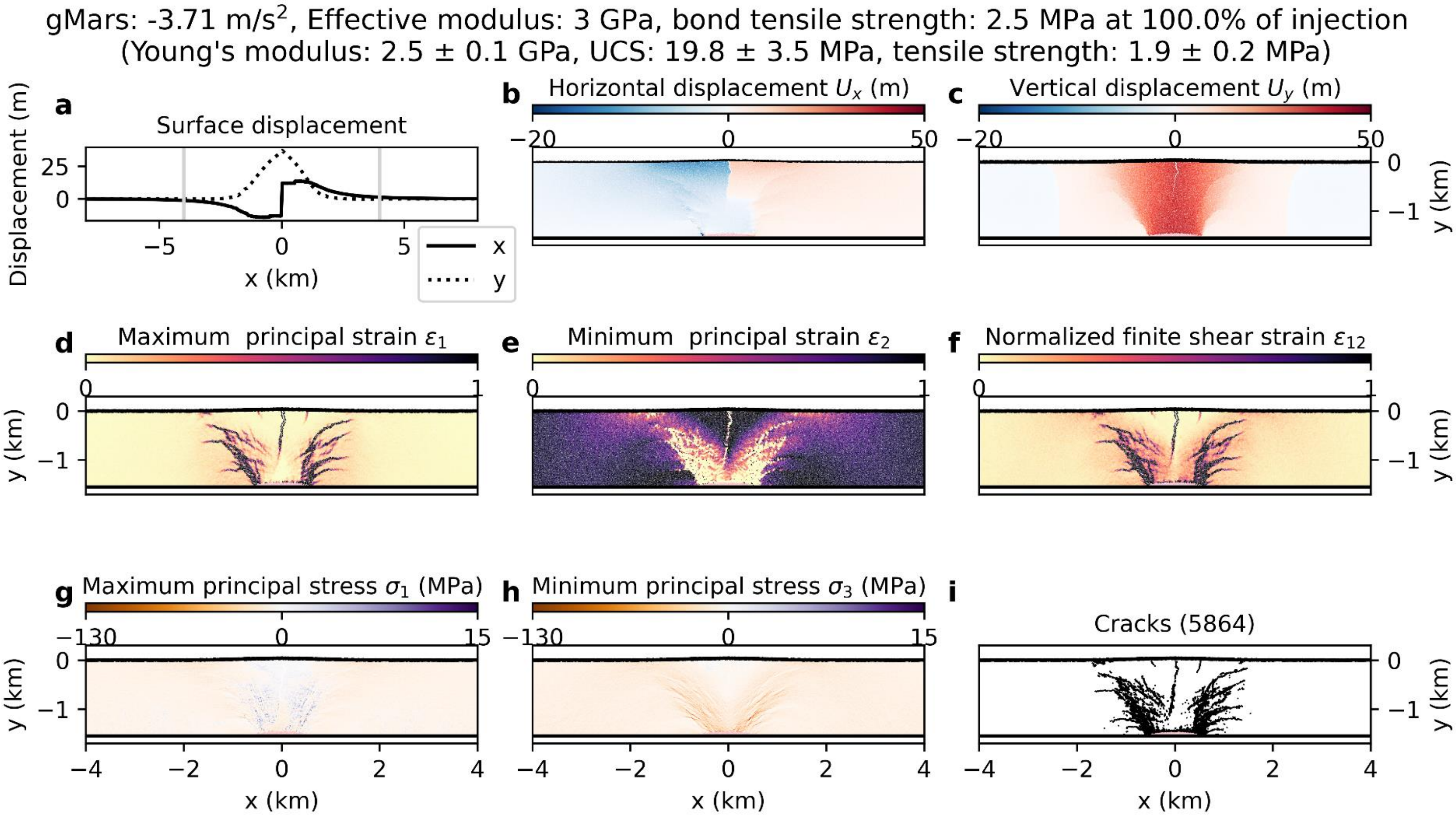

Figure S05. Deformation components at 100% of laccolith pressurization on Mars: (a) horizontal x and vertical y surface displacement; (b) horizontal displacement; (c) vertical displacement; (d) maximum principal strain; (e) minimum principal strain; (f) normalized finite shear strain; (g) maximum principal stress; (h) minimum principal stress; (i) broken particle bonds (cracks) as black lines. See Text S2 above for details on the cutoff on displacements (b, c), strains (d, e, f), and stresses (g, h).

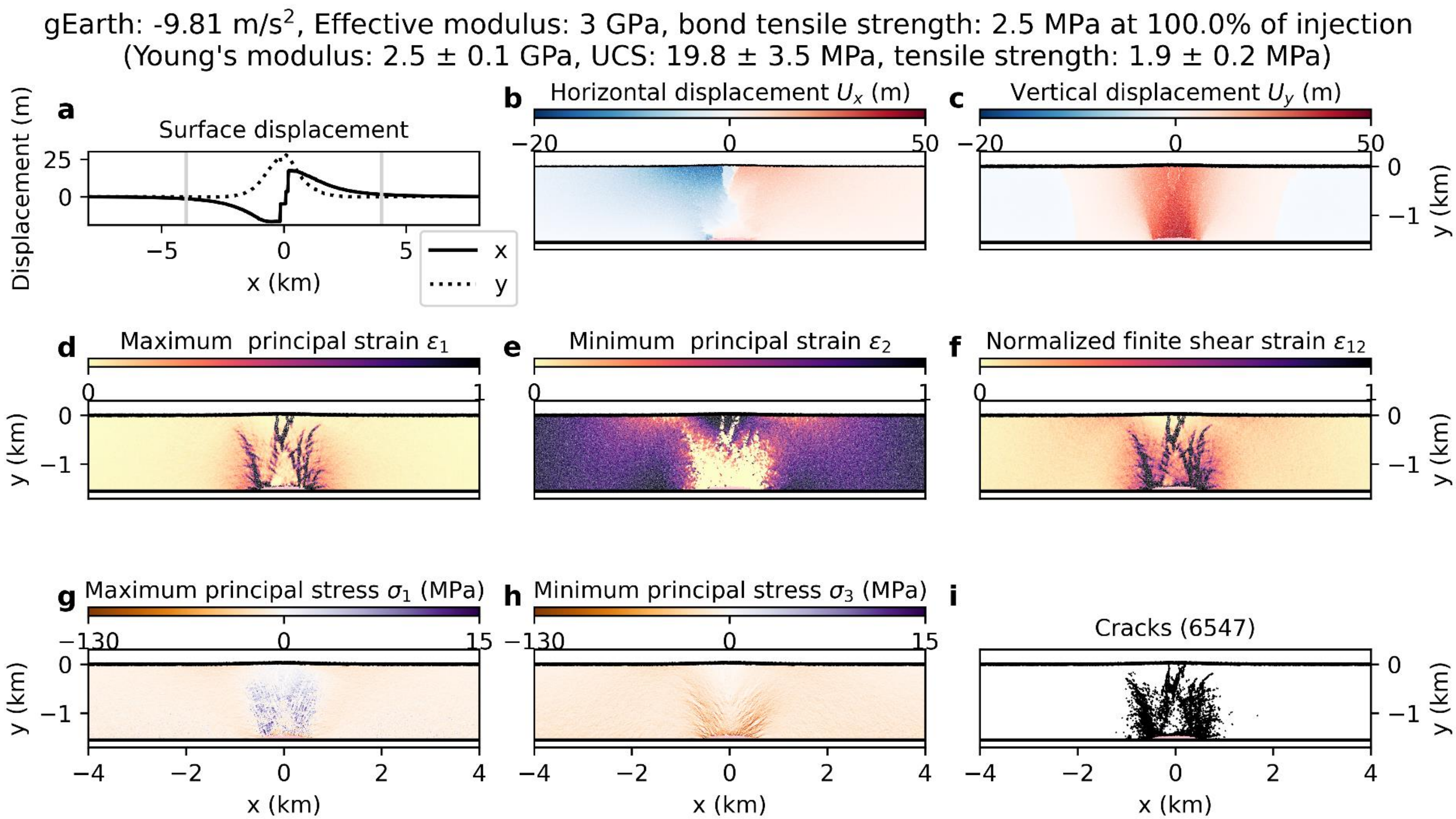

Figure S06. Deformation components at 100% of laccolith pressurization on Earth: (a) horizontal x and vertical y surface displacement; (b) horizontal displacement; (c) vertical displacement; (d) maximum principal strain; (e) minimum principal strain; (f) normalized finite shear strain; (g) maximum principal stress; (h) minimum principal stress; (i) broken particle bonds (cracks) as black lines. See Text S2 above for details on the cutoff on displacements (b, c), strains (d, e, f), and stresses (g, h).

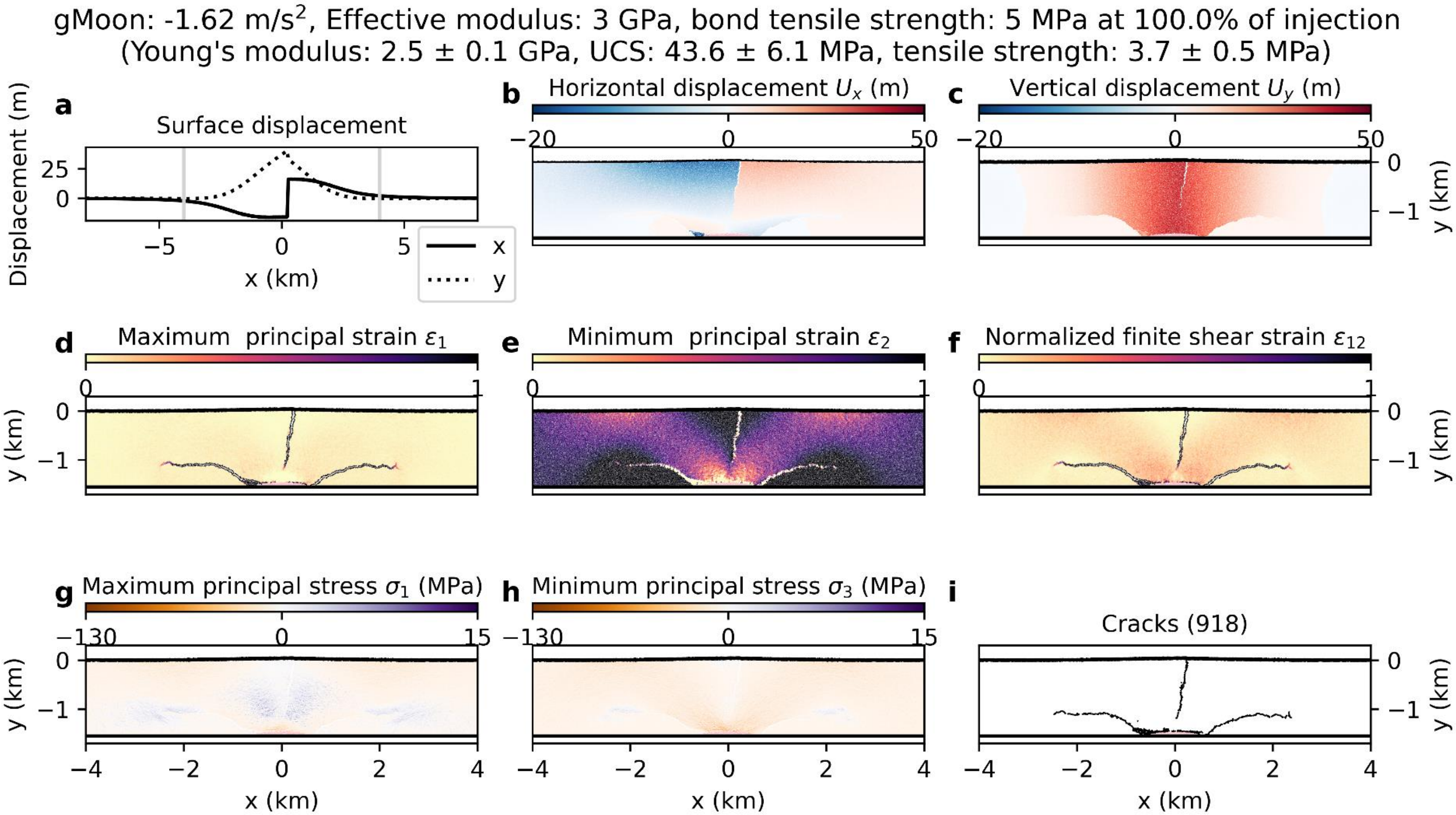

Figure S07. Deformation components at 100% of laccolith pressurization on the Moon: (a) horizontal x and vertical y surface displacement; (b) horizontal displacement; (c) vertical displacement; (d) maximum principal strain; (e) minimum principal strain; (f) normalized finite shear strain; (g) maximum principal stress; (h) minimum principal stress; (i) broken particle bonds (cracks) as black lines. See Text S2 above for details on the cutoff on displacements (b, c), strains (d, e, f), and stresses (g, h).

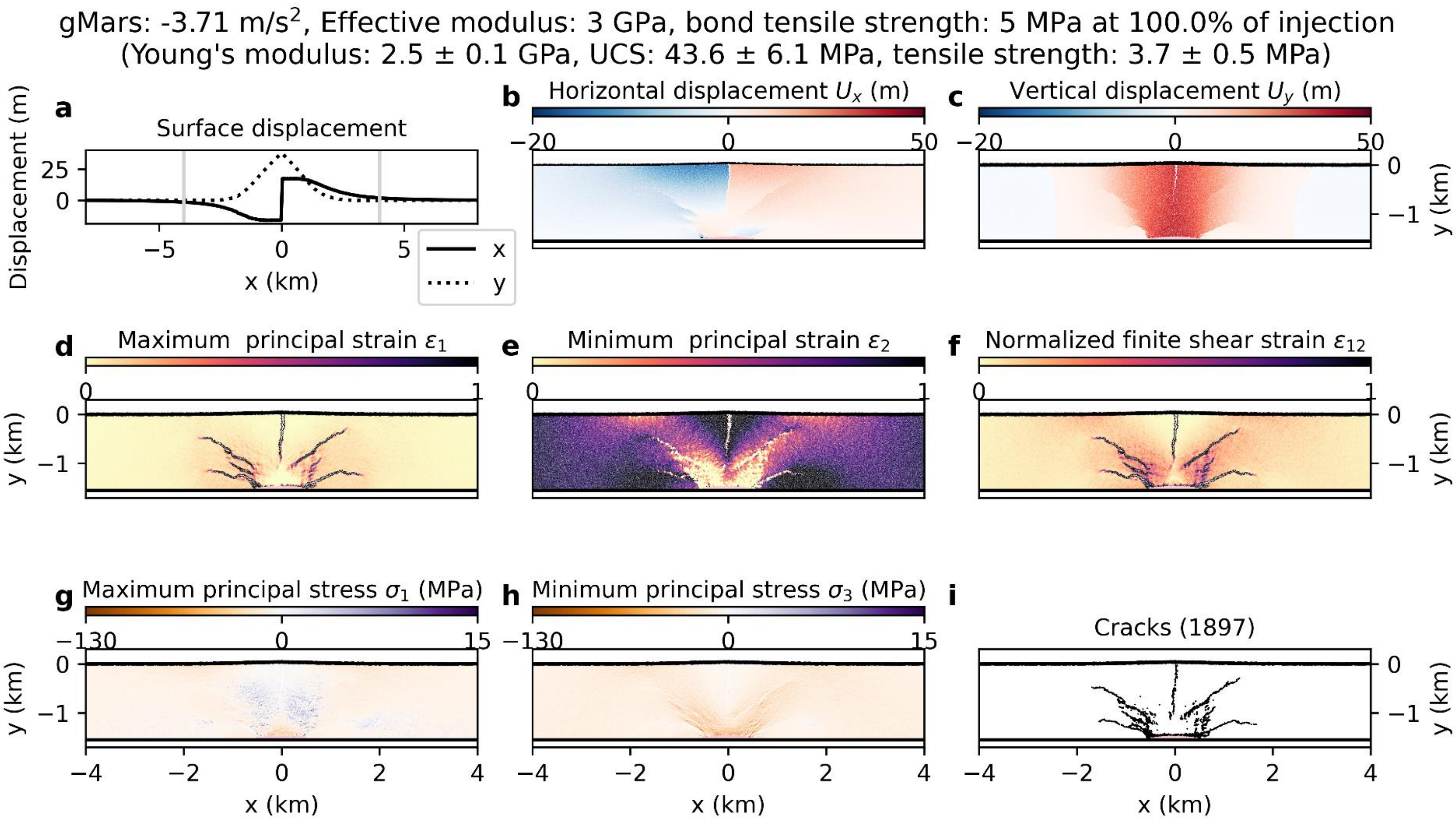

Figure S08. Deformation components at 100% of laccolith pressurization on Mars: (a) horizontal x and vertical y surface displacement; (b) horizontal displacement; (c) vertical displacement; (d) maximum principal strain; (e) minimum principal strain; (f) normalized finite shear strain; (g) maximum principal stress; (h) minimum principal stress; (i) broken particle bonds (cracks) as black lines. See Text S2 above for details on the cutoff on displacements (b, c), strains (d, e, f), and stresses (g, h).

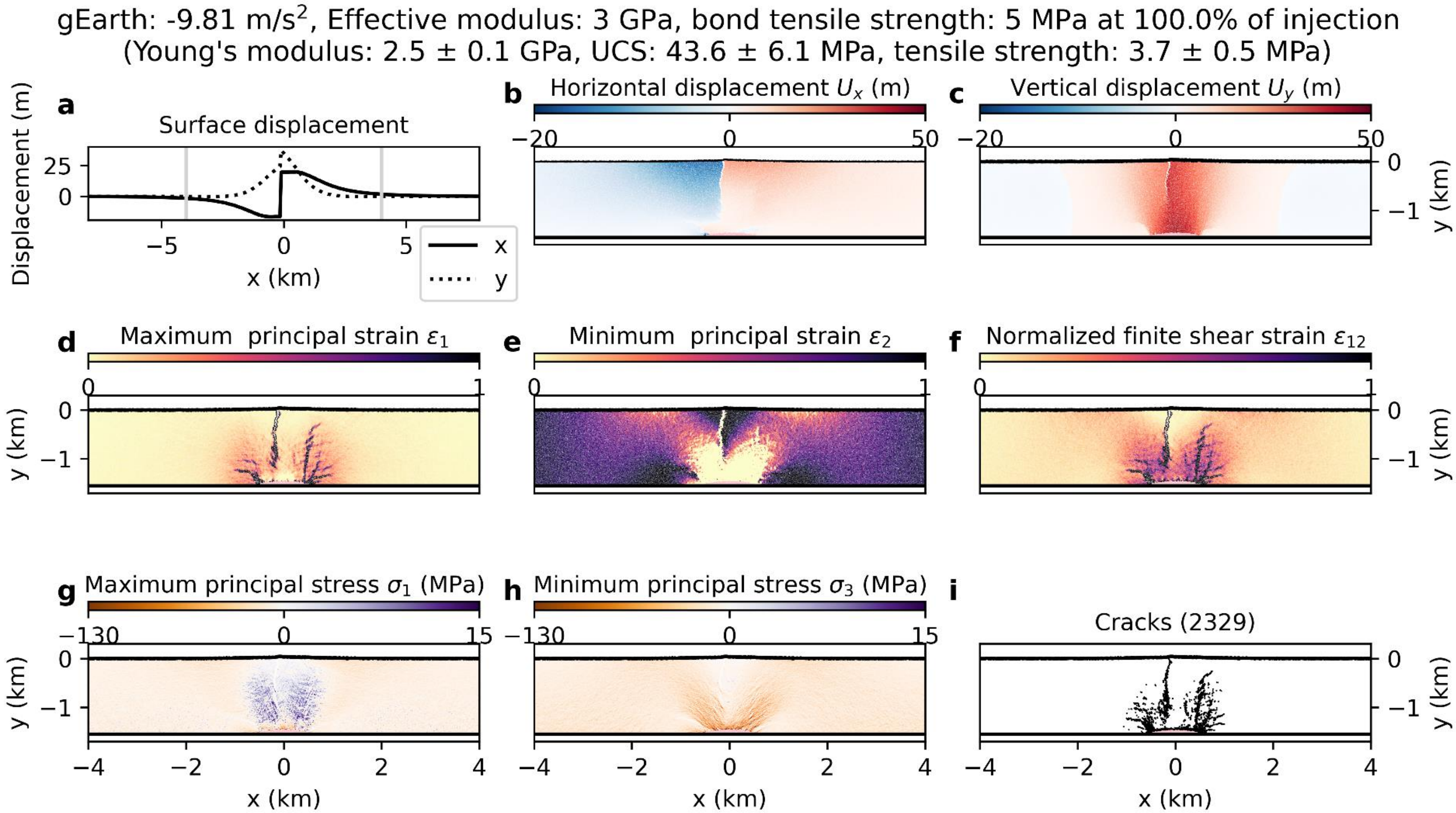

Figure S09. Deformation components at 100% of laccolith pressurization on Earth: (a) horizontal x and vertical y surface displacement; (b) horizontal displacement; (c) vertical displacement; (d) maximum principal strain; (e) minimum principal strain; (f) normalized finite shear strain; (g) maximum principal stress; (h) minimum principal stress; (i) broken particle bonds (cracks) as black lines. See Text S2 above for details on the cutoff on displacements (b, c), strains (d, e, f), and stresses (g, h).

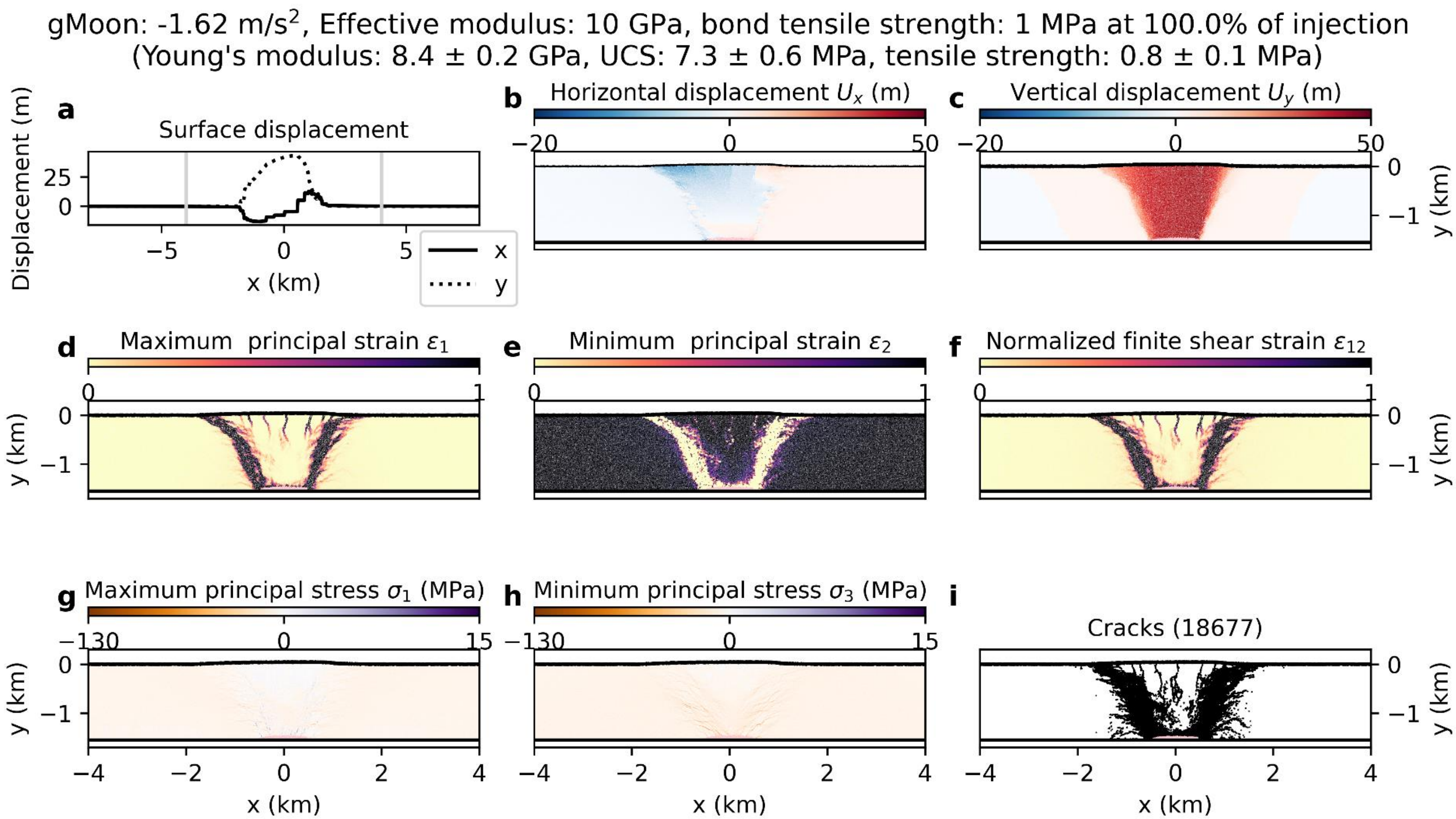

Figure S10. Deformation components at 100% of laccolith pressurization on the Moon: (a) horizontal x and vertical y surface displacement; (b) horizontal displacement; (c) vertical displacement; (d) maximum principal strain; (e) minimum principal strain; (f) normalized finite shear strain; (g) maximum principal stress; (h) minimum principal stress; (i) broken particle bonds (cracks) as black lines. See Text S2 above for details on the cutoff on displacements (b, c), strains (d, e, f), and stresses (g, h).

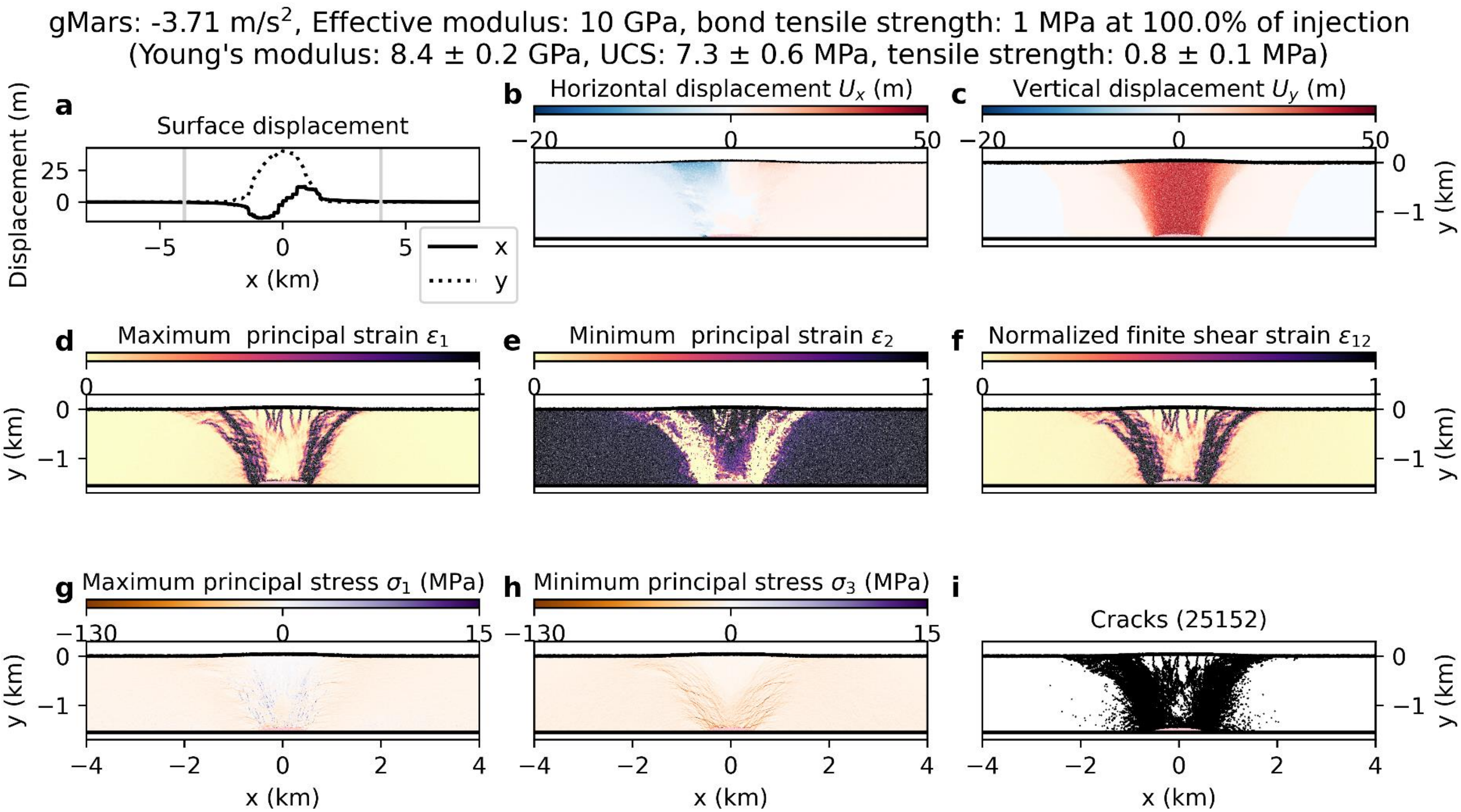

Figure S11. Deformation components at 100% of laccolith pressurization on Mars: (a) horizontal x and vertical y surface displacement; (b) horizontal displacement; (c) vertical displacement; (d) maximum principal strain; (e) minimum principal strain; (f) normalized finite shear strain; (g) maximum principal stress; (h) minimum principal stress; (i) broken particle bonds (cracks) as black lines. See Text S2 above for details on the cutoff on displacements (b, c), strains (d, e, f), and stresses (g, h).

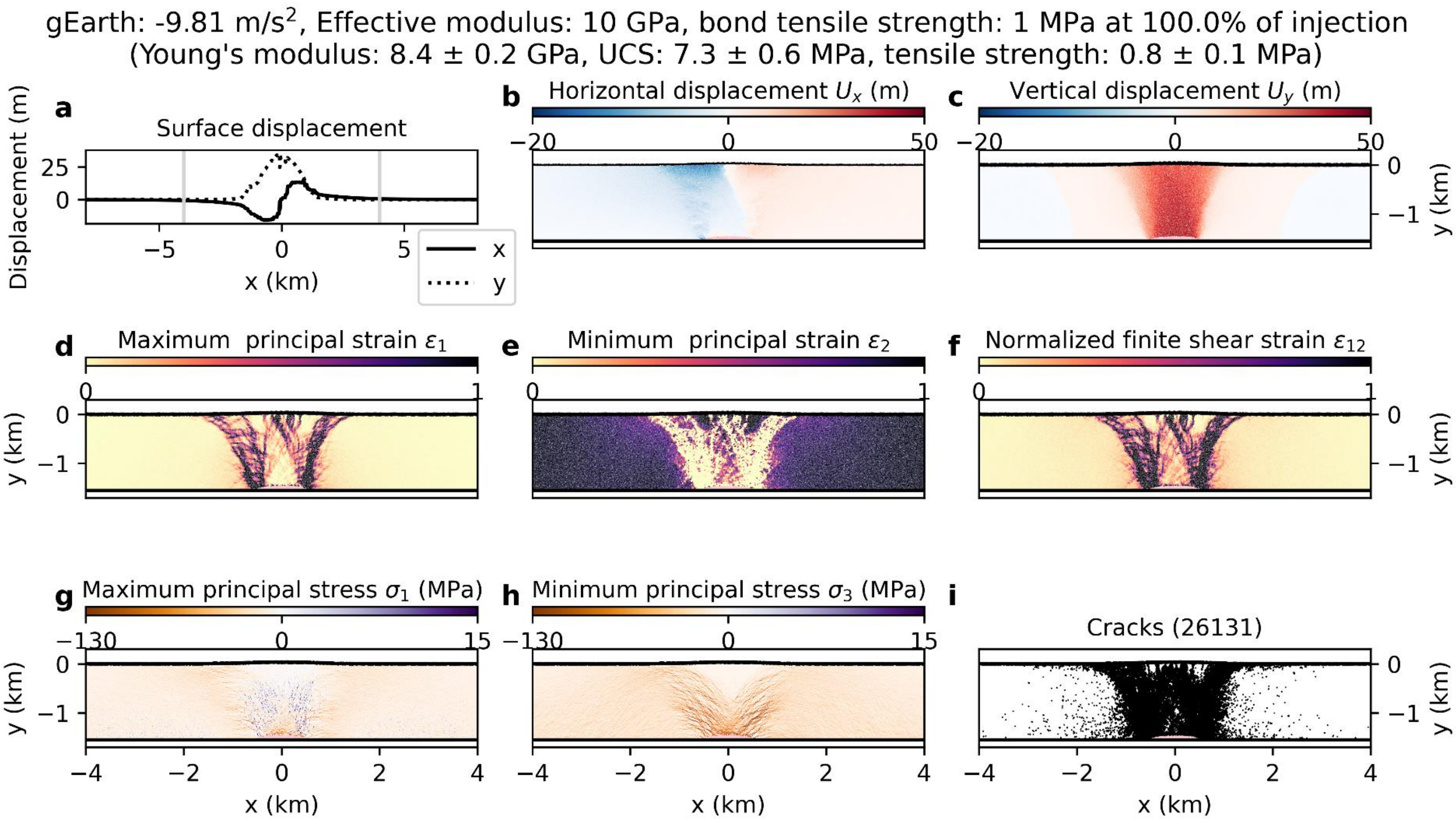

Figure S12. Deformation components at 100% of laccolith pressurization on Earth: (a) horizontal x and vertical y surface displacement; (b) horizontal displacement; (c) vertical displacement; (d) maximum principal strain; (e) minimum principal strain; (f) normalized finite shear strain; (g) maximum principal stress; (h) minimum principal stress; (i) broken particle bonds (cracks) as black lines. See Text S2 above for details on the cutoff on displacements (b, c), strains (d, e, f), and stresses (g, h).

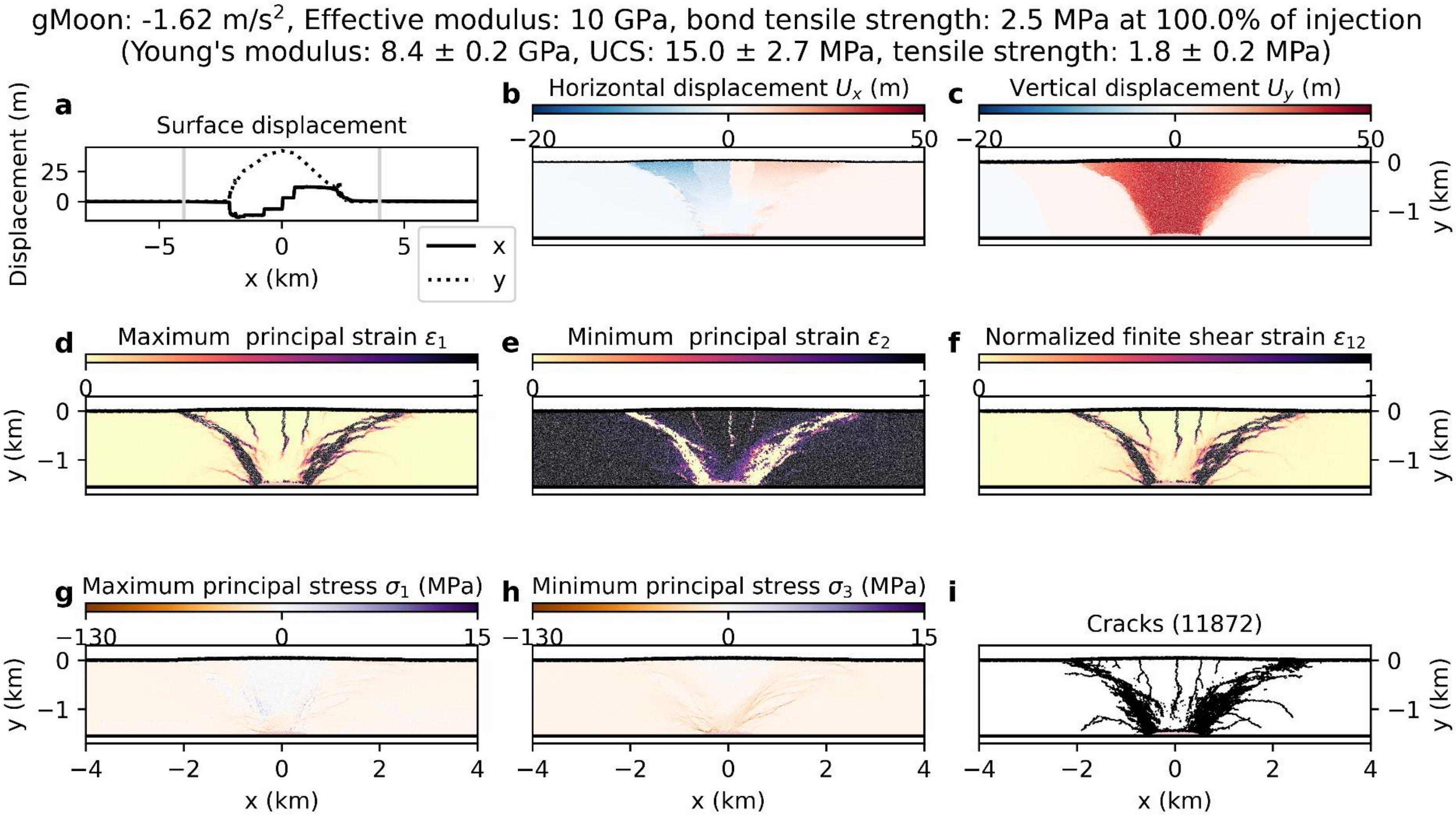

Figure S13. Deformation components at 100% of laccolith pressurization on the Moon: (a) horizontal x and vertical y surface displacement; (b) horizontal displacement; (c) vertical displacement; (d) maximum principal strain; (e) minimum principal strain; (f) normalized finite shear strain; (g) maximum principal stress; (h) minimum principal stress; (i) broken particle bonds (cracks) as black lines. See Text S2 above for details on the cutoff on displacements (b, c), strains (d, e, f), and stresses (g, h).

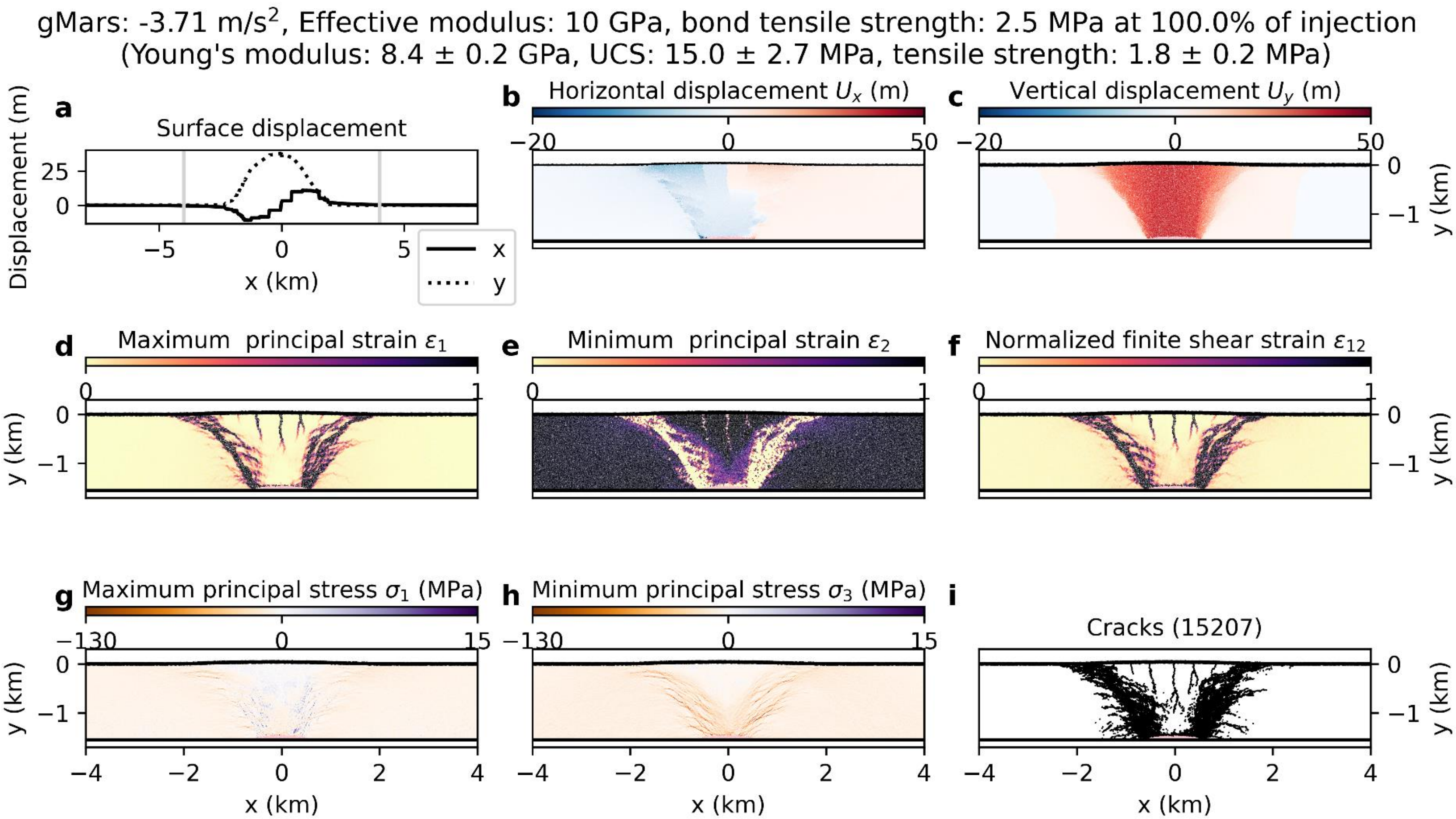

Figure S14. Deformation components at 100% of laccolith pressurization on Mars: (a) horizontal x and vertical y surface displacement; (b) horizontal displacement; (c) vertical displacement; (d) maximum principal strain; (e) minimum principal strain; (f) normalized finite shear strain; (g) maximum principal stress; (h) minimum principal stress; (i) broken particle bonds (cracks) as black lines. See Text S2 above for details on the cutoff on displacements (b, c), strains (d, e, f), and stresses (g, h).

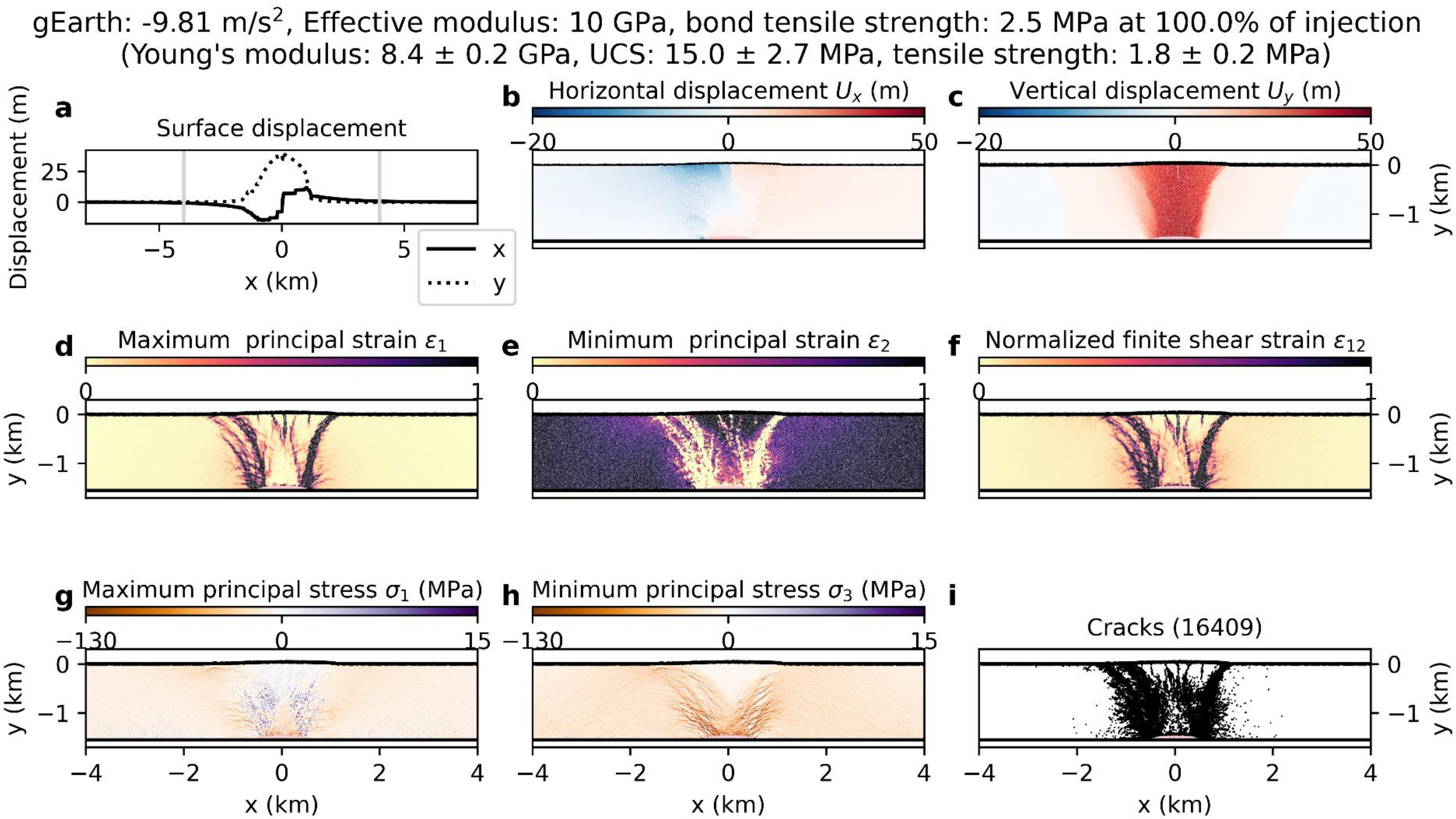

Figure S15. Deformation components at 100% of laccolith pressurization on Mars: (a) horizontal x and vertical y surface displacement; (b) horizontal displacement; (c) vertical displacement; (d) maximum principal strain; (e) minimum principal strain; (f) normalized finite shear strain; (g) maximum principal stress; (h) minimum principal stress; (i) broken particle bonds (cracks) as black lines. See Text S2 above for details on the cutoff on displacements (b, c), strains (d, e, f), and stresses (g, h).

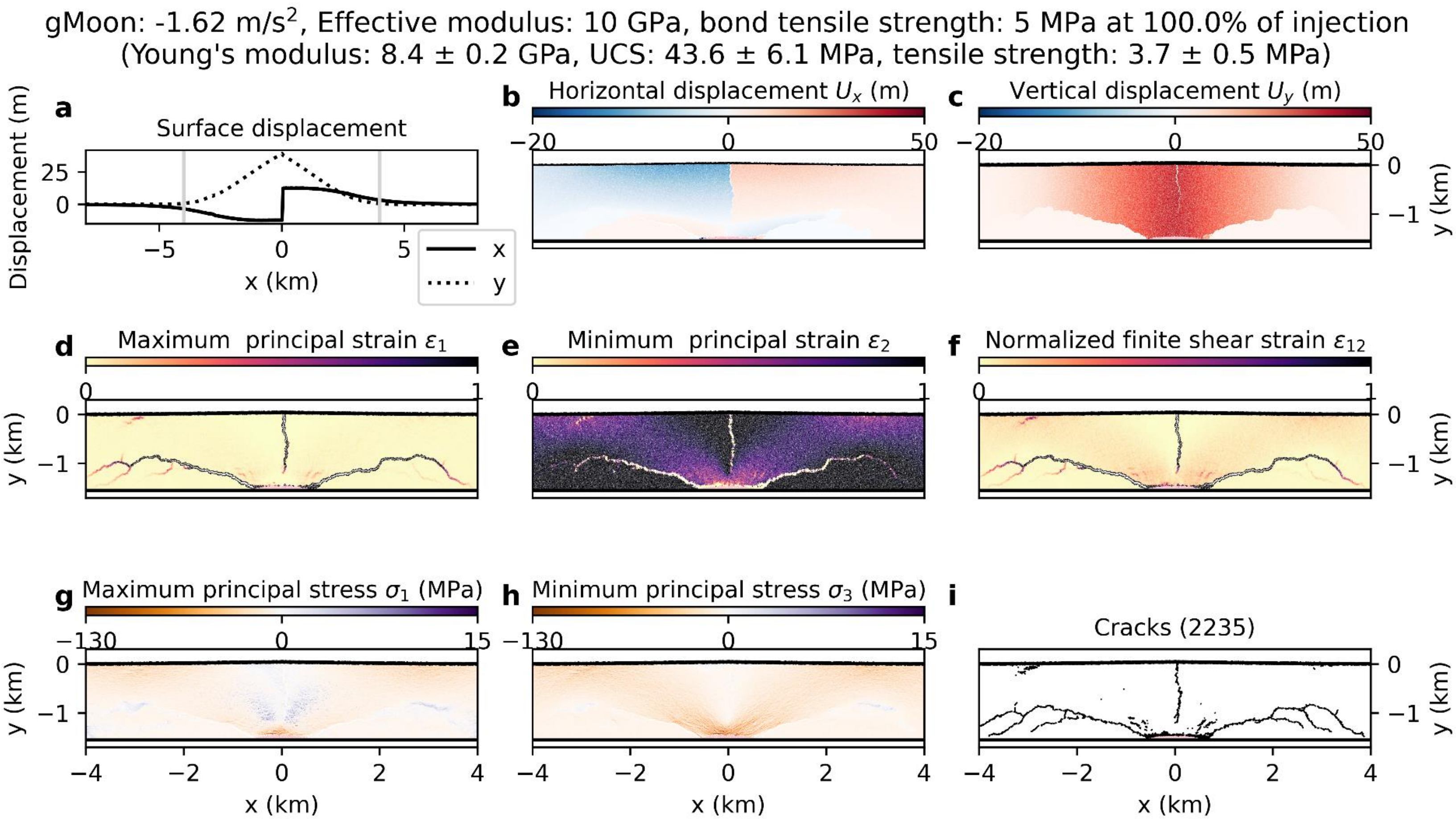

Figure S16. Deformation components at 100% of laccolith pressurization on the Moon: (a) horizontal x and vertical y surface displacement; (b) horizontal displacement; (c) vertical displacement; (d) maximum principal strain; (e) minimum principal strain; (f) normalized finite shear strain; (g) maximum principal stress; (h) minimum principal stress; (i) broken particle bonds (cracks) as black lines. See Text S2 above for details on the cutoff on displacements (b, c), strains (d, e, f), and stresses (g, h).

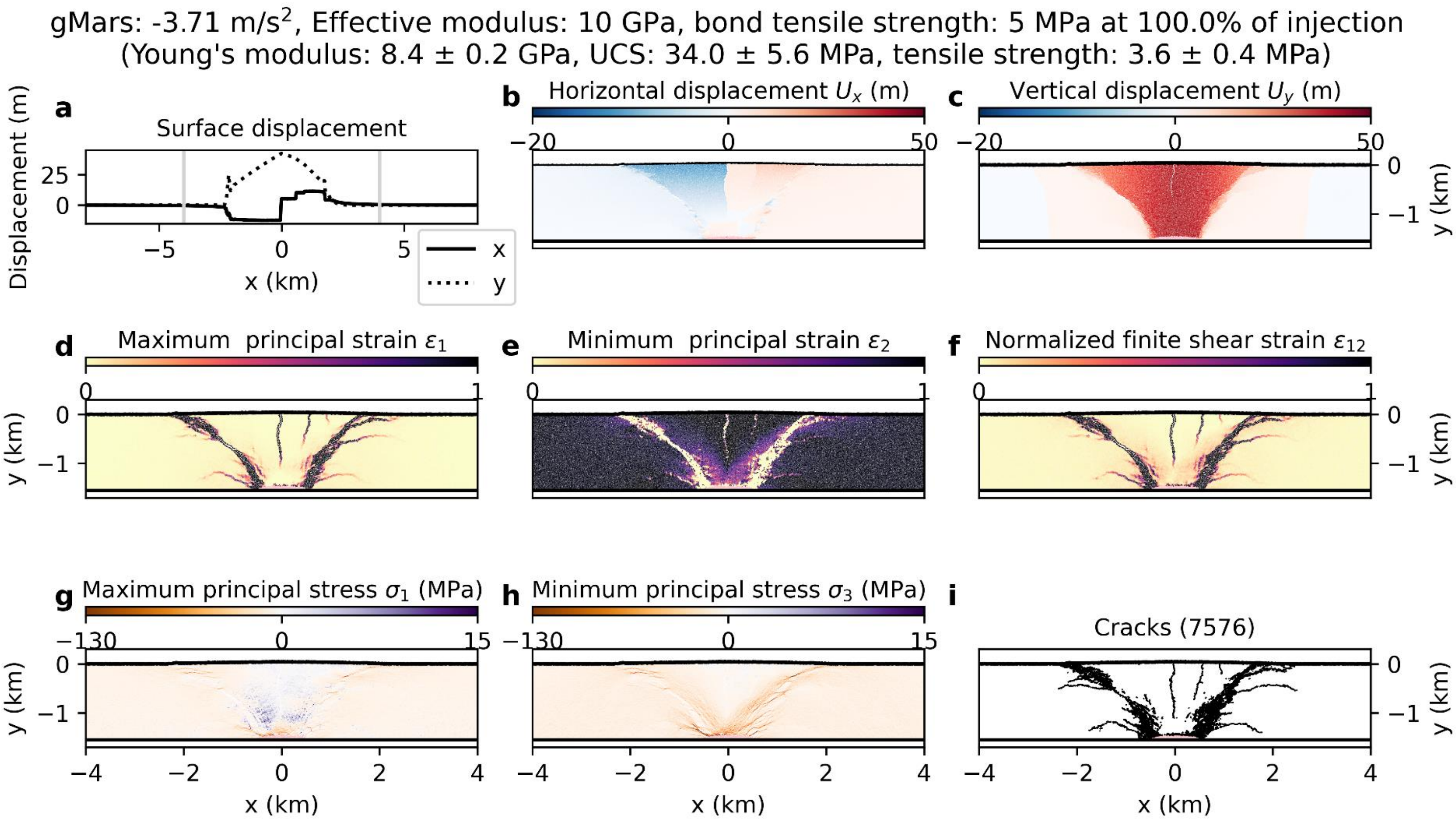

Figure S17. Deformation components at 100% of laccolith pressurization on Mars: (a) horizontal x and vertical y surface displacement; (b) horizontal displacement; (c) vertical displacement; (d) maximum principal strain; (e) minimum principal strain; (f) normalized finite shear strain; (g) maximum principal stress; (h) minimum principal stress; (i) broken particle bonds (cracks) as black lines. See Text S2 above for details on the cutoff on displacements (b, c), strains (d, e, f), and stresses (g, h).

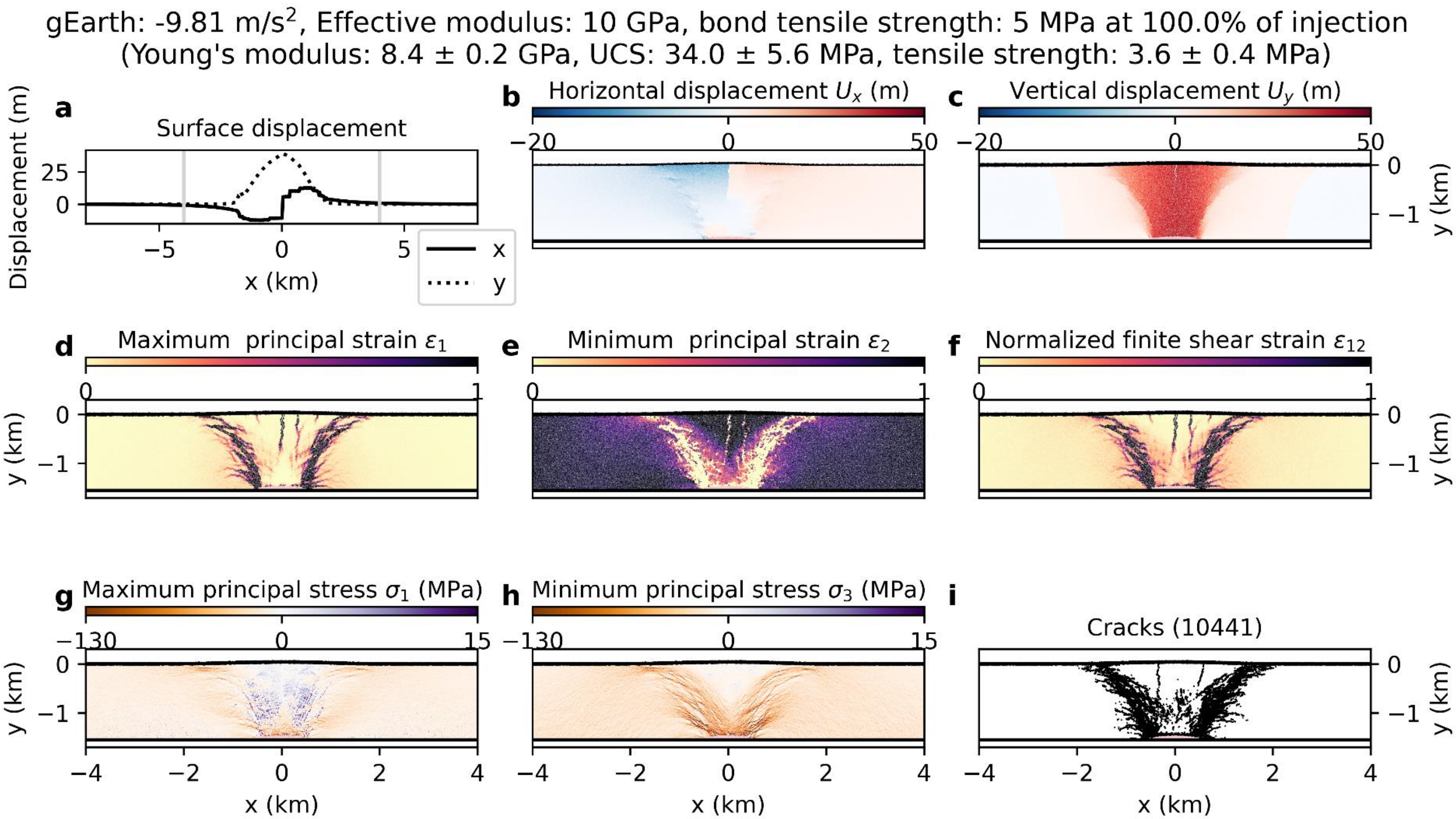

Figure S18. Deformation components at 100% of laccolith pressurization on Earth: (a) horizontal x and vertical y surface displacement; (b) horizontal displacement; (c) vertical displacement; (d) maximum principal strain; (e) minimum principal strain; (f) normalized finite shear strain; (g) maximum principal stress; (h) minimum principal stress; (i) broken particle bonds (cracks) as black lines. See Text S2 above for details on the cutoff on displacements (b, c), strains (d, e, f), and stresses (g, h).

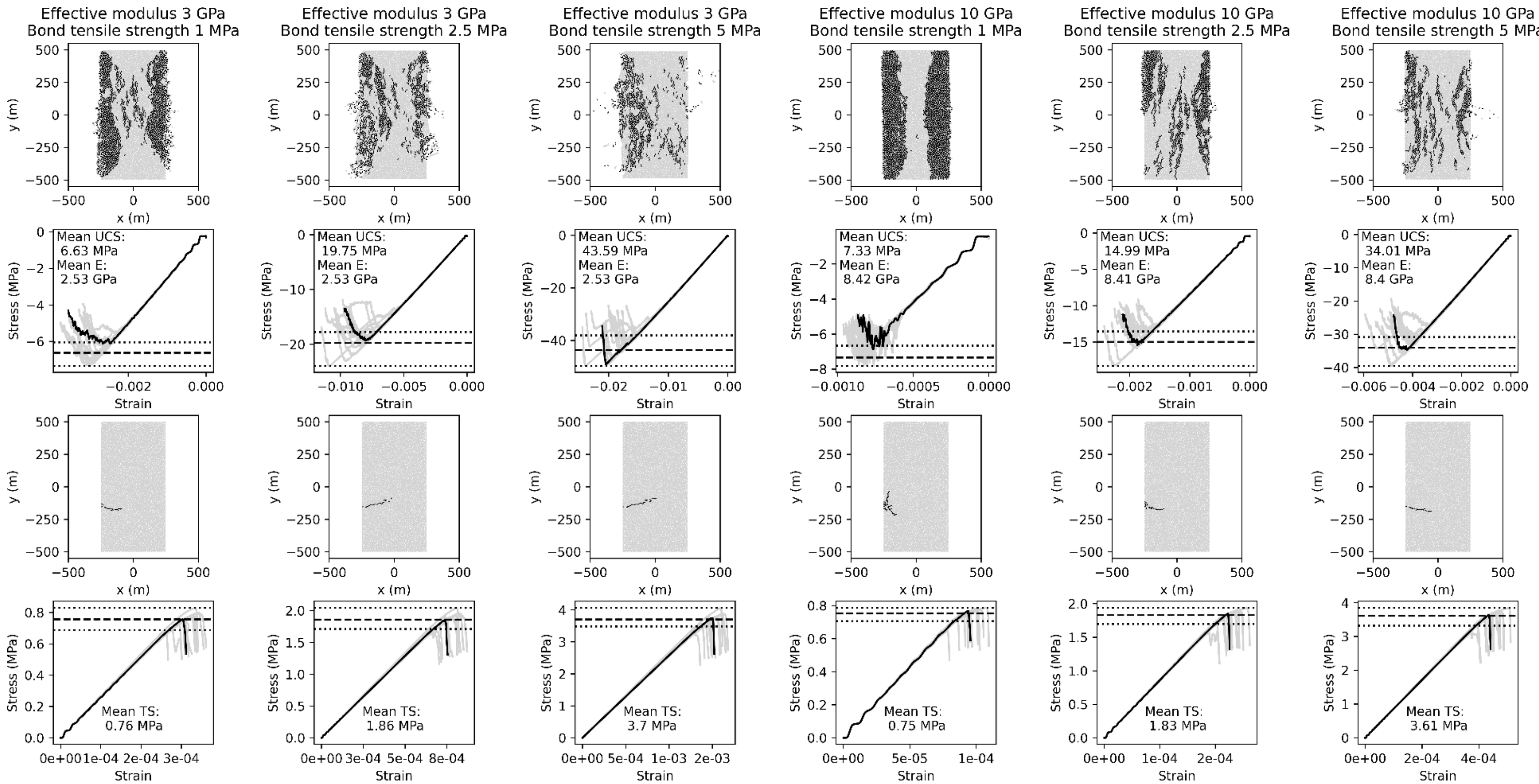

Figure S19. Results of 15 uniaxial compressive (rows 1-2) and tensile (rows 3-4) load experiments performed on each of six particle assemblages in PFC2D, to determine the assemblage´s bulk Young's modulus (E), unconfined compressive strength (UCS) and tensile strength (TS) from the stress-strain response (rows 2 and 4). Small black lines perpendicular to bonds in rows 1 and 3 represent broken contacts. Grey curves in rows 2 and 4 correspond to 15 uniaxial experiments; black curves correspond to the result of one individual test shown per particle bond strength in rows 1 and 3.

Tables

Model geometry	
Model width	20,000 m
Depth of laccolith top	1,000 m
Laccolith width	1,000 m
Laccolith height	50 m
Particle radii	6.65 ± 1.65 m
Number of particles	~120 x 10^3
PFC2D7 contact model	
Rock-rock	Soft-bond
Rock-wall	Soft-Bond
Magma-magma	Linear parallel bond
Magma-wall	Linear
Magma-rock	Linear parallel bond
Along broken bonds (cracks)	Rolling resistance linear
Bond parameters that control stiffness	
Effective modulus (E*)	2.5 x 10^9 (Pa) $^{\alpha}$
Ratio between normal and shear stiffness	2.5
Bond parameters that control toughness	
Bond tensile strength (ten)	0.0 (Pa) $^{\alpha}$
Bond cohesion (coh)	10 x bond tensile strength (Pa)
Other contact parameters	
Friction angle	Rock-rock/rock-wall: 30.0 (°) Rock-magma: 26.6 (°) Other bonds: 0.0 (°)
Friction coefficient between unbonded particles	Magma-magma/magma-wall: 0.0 Other bonds: 0.5
Softening factor (γ)	Rock-rock/rock-wall: 13
Softening tensile strength factor (ζ)	Rock-rock/rock-wall: 0.4
Radius multiplier	1.0
Gap between bonded particles	6.65 x 10^{-3} (m)

$^{\alpha}$ *for rock-rock bonds and rock-wall bonds, see Table 1 in the main text.*

Table S1. Constant computational parameters in the 2D DEM models in PFC2D.